Linear stability analysis of fluid–structure interaction problems with an immersed boundary method

Antonia Tirri [a], Alessandro Nitti [a], Javier Sierra-Ausin [b,c], Flavio Giannetti [b], Marco D. de Tullio [a,*]

[a] *Department of Mechanics Mathematics and Management, Polytechnic University of Bari, Via Re David 200, Bari, 70125, Italy*
[b] *Department of Industrial Engineering, University of Salerno, Via Giovanni Paolo II 132, Fisciano, 84084, Italy*
[c] *Institut de Mécanique des Fluides de Toulouse - IMFT, 2 allée du Pr. Camille Soula, Toulouse, 31400, France*

ARTICLE INFO

ABSTRACT

In this work, we present a novel approach to perform the linear stability analysis of fluid–structure interaction problems. The underlying idea is the combination of a validated immersed boundary solver for the nonlinear coupled dynamics with Krylov-based techniques to obtain a robust and accurate global stability solver for elastic structures interacting with incompressible viscous flows. The computation of the leading eigenvalues of the linearized system is carried out in a matrix-free framework by adopting a classical Krylov subspace method. The proposed algorithm avoids the complex analytical linearization of the equations while retaining all the relevant aspects of the fully-coupled fluid–structure system.

The methodology has been tested for several cases involving two-dimensional incompressible flows around elastically mounted circular cylinders. The obtained results show a good quantitative agreement with those available in the literature. Finally, the method was applied to investigate the linear stability of the laminar flow past two elastically mounted cylinders in tandem configuration at $Re = 100$, revealing the existence of two complex dominant modes. For low values of the reduced velocity U^*, only one mode is found to be unstable and related to the stationary wake mode. The loss of stability of the second mode at $U^* = 4$ marks the beginning of the lock-in region. We also show that for $U^* = 5$ the modes interact, giving rise to the beating phenomenon observable in the nonlinear time evolution of the system. For larger values of the reduced velocity, the linear dynamics is governed by one dominant mode characterized by wider oscillations of the rear cylinder, matching the results of the nonlinear simulations.

© 2022 Elsevier Ltd. All rights reserved.

1. Introduction

The interaction of elastic bodies with incompressible flows has attracted the interest of many researchers since the pioneering studies on aeroelasticity (Theodorsen, 1934; Kornecki et al., 1976). These configurations are encountered in a large variety of engineering applications, spanning from biomedical devices (de Tullio et al., 2009; Borazjani, 2013) to energy harvesting systems (Doaré and Michelin, 2011; Grouthier et al., 2014; Nitti et al., 2022) and unmanned underwater vehicles (Tangorra et al., 2007; Mansoorzadeh and Javanmard, 2014). Such systems are prone to several types of instability

---

* Corresponding author.
   E-mail address: marcodonato.detullio@poliba.it (M.D. de Tullio).

and, despite their complex nonlinear behavior, the early stages of the transition between two distinct dynamical states can often be explained in terms of the excitation of a linearly unstable mode. While being a well-established technique for investigating fluid flows (Theofilis, 2011), linear stability analysis (LSA) has been adopted quite recently for cases involving fully coupled fluid–structure interactions (FSI), mainly to provide insights into the physical mechanisms associated with the emergence of flow-induced oscillations and to design control strategies able to suppress them.

The first examples of linear stability analyses over FSI configurations date back to the pivotal studies of Theodorsen (1934) on the flutter instability of an aerodynamic section. Theodorsen formulation was based on the potential flow and slender body assumptions. While the adoption of these simplified flow models is legitimate in the field of classical aeronautics, applications involving low to medium Reynolds numbers or flow separation require the simultaneous solution of the linearized Navier–Stokes equations coupled with the linearized equation of motion of the elastic solid.

Cossu and Morino (2000) were the first to perform a linear stability analysis of a two-dimensional low Reynolds number flow interacting with an elastically-mounted bluff body. They investigated the primary instability of a circular cylinder, which was free to oscillate in the cross-flow direction by solving the linearized flow equations in a moving reference frame. Navrose and Mittal (2016) adopted the same approach with a non-inertial frame of reference to conduct a parametric study of the lock-in phenomenon exhibited by elastically-mounted circular cylinders in the laminar flow regime. Cossu and Morino (2000) reported a critical Reynolds number half the value obtained for the fixed cylinder case with low solid-to-fluid density ratios. Meliga and Chomaz (2011) extended the stability analyses to smaller mass ratios ($\mathcal{O}(10^{-4})$). The numerical technique employed therein consisted in a multiple-time-scale expansion to decouple fluid and solid dynamics at the leading order of the perturbation.

More recently, Pfister et al. (2019) adopted a Lagrangian-based approach to derive a linearization of the equations of motion for a coupled fluid–structure problem written in an Arbitrary-Lagrangian–Eulerian (ALE) framework. This formulation becomes cumbersome when it is based on the Lagrangian motion of the structure, requiring important modifications in the residual o the Navier–Stokes equations to take into account the motion of the mesh. Fernández and Le Tallec (2002) proposed, instead, an Eulerian-based formulation in an attempt to overcome the difficulties arising from a moving grid. In their formulation, obtained starting from the weak form of the ALE equations, the coupling between the flow and the solid is made via a transpiration technique. Although reducing considerably the complexity of the problem, this method produces additional stress contributions at the interface, termed *added stiffness*, that depend on higher-order derivatives of the flow variables. Negi et al. (2020) followed the same methodology but performed the linearization of the equations of motion in their integral form.

Moulin et al. (2017) suggested the use of non-conforming methods to investigate the stability of strongly coupled FSI systems, discussing, in particular, the adoption of a fictitious domain formulation to handle the coupling between the fluid and the solid. Goza et al. (2018), who also proposed a non-conforming approach, conducted a global stability analysis of inverted flags submerged in uniform flows using an Immersed Boundary (IB) method. They resorted to the numerical derivation of the Jacobian matrix linearizing the discretized operators around the steady state via a first-order finite difference scheme. The memory requirements with matrix-forming strategies become rapidly unfeasible when dealing with a large number of degrees of freedom, e.g., three-dimensional FSI configurations. This aspect is even more relevant in the computation of neutral curves since the Jacobian matrix must be re-evaluated for each base flow.

In this work, we propose an alternative procedure to study the linear stability characteristics of FSI systems by adopting a Jacobian-free approach (Mettot et al., 2014). Matrix-free strategies lead to significant memory savings at the cost of longer integration times. In contrast, they provide access to only a subset of the spectrum associated with the eigenvalue problem (EVP) that originates from the classic normal-mode approach. Nonetheless, the accessible portion of the spectrum is generally the most relevant, consisting of the most unstable eigenvalues.

In the present article, we adopt a time-stepping methodology that makes use of high-fidelity nonlinear simulations obtained with a direct-forcing IB method, based on a moving-least-square (MLS) approach. One of the main advantages of the IB formulation resides in the fact that it can handle multi-body configurations with no additional complexity. In addition, the fluid equations are resolved on a staggered Cartesian grid, which makes the method prone to a simple parallel implementation for three-dimensional computations.

The choice of the specific IB forcing technique is crucial for the success of the computation. It has been noted that the use of a sharp forcing field usually leads to the appearance of unphysical fluctuations of the hydro-dynamical force acting on the solid body (Uhlmann, 2003). Seo and Mittal (2011) attribute the emergence of pressure oscillations to an unintended *transpiration* effect at the immersed boundary, due to the fact that the role of the Eulerian nodes close to the interface can change from a time-step to the next as the body moves. These spurious oscillations can be suppressed by spreading the forcing term over a wider stencil through the use of a smoother Lagrangian–Eulerian transfer function (Yang et al., 2009). In view of these considerations, and after a few trials, we adopted an MLS forcing procedure that provides a good trade-off between accuracy and robustness. Details on the IB treatment are provided in the next section.

The proposed strategy involves the adoption of the matrix exponential, first introduced by Eriksson and Rizzi (1985) in the context of global stability analysis. In their paper, the authors proposed to approximate the action of the Jacobian matrix via finite differences to investigate the instability of the transonic flow over an airfoil, a phenomenon modeled by the two-dimensional Euler equations. They also highlighted the need for a matrix transformation to retrieve the least stable portion of the spectrum of the discrete operator. The same approach was later extended to the full Navier–Stokes equations by Chiba (1998), who performed a linear stability analysis of the two-dimensional square lid-driven cavity flow,

and by Tezuka and Suzuki (2006), who carried out a TriGlobal stability analysis (Theofilis and Colonius, 2011) of the flow around various spheroids.

Gómez et al. (2011) incorporated the approach of Tezuka and Suzuki (2006) into publicly-available computational fluid dynamics (CFD) solvers, highlighting the flexibility of the method that looks at the CFD solver as a black-box source. In a successive paper (Gómez et al., 2015), Gomez et al. extended that work by inserting a shift-invert strategy to grant access to specific portions of the spectrum. Our contribution builds on the above-mentioned series of papers and provides an extension of Chiba's approach to FSI problems.

This paper is organized as follows. First, in Section 2, we introduce the problem of linear stability in the context of fluid–structure interaction and derive the theoretical foundations of the methodology. Numerical validation of the solver is presented in Section 3, together with the results obtained by applying the presented strategy to the problem of flow-induced vibrations of two cylinders in tandem. In Section 4, the main results and conclusions are summarized.

2. Methodology

In this work, the discussion is restricted to the motion of elastically-mounted rigid bodies immersed in a two-dimensional incompressible viscous flow, although the derived method remains completely general.

2.1. Governing equations

The governing equations of the flow dynamics are the incompressible Navier–Stokes equations, written in the dimensionless form:

$$\frac{\partial \boldsymbol{u}}{\partial t} + \boldsymbol{u} \cdot \nabla \boldsymbol{u} = -\nabla p + \frac{1}{Re} \nabla^2 \boldsymbol{u} + \boldsymbol{f}, \tag{1}$$
$$\nabla \cdot \boldsymbol{u} = 0,$$

where $\boldsymbol{u}$ and p denote the fluid velocity and pressure, respectively. The body force term $\boldsymbol{f}$, in the absence of other external fields, corresponds to the IB body-force field. Eq. (1) is closed by appropriate boundary conditions related to the specific considered configuration. Flow variables have been made dimensionless by considering a reference length L_r and velocity scale U_r; the Reynolds number is defined as $Re = (U_r L_r)/\nu$, with ν the kinematic viscosity of the fluid.

The structure is modeled as a rigid body with the elastic center coincident with the center of mass. Its motion is governed by Newton's second law for the ith degree of freedom:

$$\ddot{x}_i + \frac{\sigma_i}{A_i^* \rho^*} \dot{x}_i + \frac{k_i}{A_i^* \rho^*} \left(x_i - x_i^{eq} \right) = C_i, \quad i = 1, \ldots, n_{DOF} \tag{2}$$

where the variables have been made dimensionless by means of the bulk parameters of the flow field.

The system of equations given by (2) represents a spring–mass–damper system where σ_i and k_i are, respectively, the non-dimensional linear damping and stiffness coefficients of the ith degree of freedom (DOF), x_i^{eq} is the equilibrium position of the ith spring and n_{DOF} gives the total number of degrees of freedom. For instance, $n_{DOF} = 3$ in two-dimensional problems, comprising the two components of the displacement and the rigid rotation around the center of mass. The term $A_i^* \rho^*$ represents the non-dimensional mass coefficient. In two dimensions, for the translational DOFs, A_i^* corresponds to A^*, which is the ratio of the cross-sectional area of the body to the square of the reference length, L_r. For the rotational DOF, $A_i^* = I^*$, which is the second moment of area with respect to the centroidal axis divided by the fourth power of L_r. The coefficient C_i represents the non-dimensional force (or torque) acting upon the ith DOF.

In the examples illustrated throughout this work, the effect of gravity has been neglected and the only contribution to the forcing term in the body equations comes from the interaction with the flow. That being the case, the behavior of a rigid body with only one degree of freedom is governed by two dimensionless parameters: the density ratio $\rho^* = \rho_s/\rho_f$, which is the ratio of solid to fluid density, and the reduced velocity $U^* = \sqrt{(A_1^* \rho^* 4\pi^2)/k_1}$, representing the ratio of two characteristic time scales of the problem, i.e., the period of the natural mode of the body and that of the convective motions of the flow.

2.2. Time stepping - Pressure-segregation algorithm

The Navier–Stokes equations (1) are integrated in time through a semi-implicit procedure (Nitti et al., 2020), where the convective and viscous terms are discretized by a third-order Runge–Kutta (RK) and a Crank–Nicolson scheme, respectively. Each substep is resolved by means of a classical fractional-step method,

$$\begin{aligned}
\hat{\boldsymbol{u}} &= \hat{\varphi}_{\Delta t}^{[1]} \boldsymbol{u}^k, \\
\tilde{\boldsymbol{u}} &= \varphi_{\Delta t}^{[1]} \boldsymbol{u}^k, \\
\boldsymbol{u}^{k+1} &= \varphi_{\Delta t}^{[2]} \tilde{\boldsymbol{u}} = \left(\varphi_{\Delta t}^{[2]} \circ \varphi_{\Delta t}^{[1]} \right) \boldsymbol{u}^k,
\end{aligned} \tag{3}$$

where $\boldsymbol{u}^k$ is the velocity field at the kth RK substep, $\hat{\boldsymbol{u}}$ is an intermediate velocity field that does not satisfy the interface conditions, $\tilde{\boldsymbol{u}}$ is a provisional field that is globally divergence-free, but not locally, and $\boldsymbol{u}^{k+1}$ is the updated velocity field at the $(k+1)$th substep. The preliminary velocity $\hat{\boldsymbol{u}}$ is computed explicitly via the discrete flow $\hat{\varphi}_{\Delta t}^{[1]}$,

$$\hat{\varphi}_{\Delta t}^{[1]}\boldsymbol{u}^k \equiv \boldsymbol{u}^k + \Delta t \left[-\alpha^k \nabla p^k + \frac{\alpha^k}{Re}\nabla^2\boldsymbol{u}^k + \beta^k H^k + \gamma^k H^{k-1} \right], \tag{4}$$

where H represents the nonlinear terms $\boldsymbol{u} \cdot \nabla\boldsymbol{u}$ and α^k, β^k and γ^k are the coefficients of the time scheme (see Nitti et al. (2020) for details). The computed field is next used to evaluate the IB forcing $\boldsymbol{f}$, whose detailed description is left to Section 2.2.1. Then, the provisional velocity field $\tilde{\boldsymbol{u}}$ is computed by solving the Helmholtz equation

$$\left(1 - \frac{\alpha^k \Delta t}{2Re}\nabla^2 \right) \Delta\tilde{\boldsymbol{u}} = \hat{\boldsymbol{u}} - \boldsymbol{u}^k + \Delta t \boldsymbol{f}(\hat{\boldsymbol{u}}), \tag{5}$$

where $\Delta\tilde{\boldsymbol{u}} = \tilde{\boldsymbol{u}} - \boldsymbol{u}^k$. The discrete flow $\varphi_{\Delta t}^{[1]}$ is defined as

$$\varphi_{\Delta t}^{[1]}\boldsymbol{u}^k = \boldsymbol{u}^k + \left(1 - \frac{\alpha^k \Delta t}{2Re}\nabla^2 \right)^{-1} \left(\hat{\boldsymbol{u}} - \boldsymbol{u}^k + \Delta t \boldsymbol{f}(\hat{\boldsymbol{u}}) \right) \tag{6}$$

Finally, the pressure is updated according to

$$p^{k+1} = p^k + \left(1 - \frac{\alpha^k \Delta t}{2Re}\nabla^2 \right) p^*, \tag{7}$$

with the scalar quantity p^* resulting from the solution of the Poisson equation,

$$\nabla^2 p^* = \frac{\nabla \cdot \tilde{\boldsymbol{u}}}{\alpha^k \Delta t}. \tag{8}$$

The RHS of Eq. (8) enforces the continuity of the final velocity field $\boldsymbol{u}^{k+1}$, given by the discrete flow $\varphi_{\Delta t}^{[2]}$,

$$\boldsymbol{u}^{k+1} = \varphi_{\Delta t}^{[2]}\tilde{\boldsymbol{u}} \equiv \tilde{\boldsymbol{u}} - \alpha^k \Delta t \nabla p^*. \tag{9}$$

A second-order-accurate spatial discretization is achieved using centered finite differences in a non-uniform staggered Cartesian grid.

Given the time-splitting nature of the fractional-step approach, the boundary conditions at the fluid–structure interface are enforced on an intermediate non-solenoidal velocity field. This imposition is subsequently spoiled in the corrector step to enforce local continuity (Fadlun et al., 2000); however, the modification of the interface velocity caused by the correction step can be minimized through a repetition of the forcing procedure after the solution of the Helmholtz equation (5). Observations have shown that the discrepancy between the interpolated final fluid velocity and the local body velocity is effectively reduced with three to five iterations of the forcing procedure (Breugem, 2012), up to a root-mean-square error equal to $\sim \mathcal{O}(10^{-5})$.

Within the present method, the local difference between the interpolated fluid velocity and the solid velocity employed in the forcing stage is measured downstream of the time-scheme, and its Root Mean Square (RMS) is evaluated over the set of Lagrangian markers (see Section 2.2.1). In presence of moving surfaces, the RMS error is found to be $\sim \mathcal{O}(10^{-4})$ of the freestream velocity (see fig. 11 of Nitti et al. (2020)).

The equations of motion for the rigid body are integrated in time by means of a Crank–Nicolson scheme. Within this staggered approach, at each sub-step, the fluid, and structural systems are solved in a sequential fashion: first, a low-order extrapolation for the fluid–solid interface position and velocity is employed in the IB procedure to advance the flow field in time; then the coupling between fluid and rigid-body dynamics is accomplished using the Eulerian load distribution $\boldsymbol{f}$ coming from the IB procedure to obtain the total force and moment integrals (Lācis et al., 2016; chih Lai and Peskin, 2000) in the RHS of Newton's equations (2). This procedure avoids the integration of pressure and viscous stresses on the contour of the body, circumventing the need for a reconstruction procedure. When the density ratio ρ^* is close to unity, a strong coupling of the fluid and solid solutions may be needed (Förster et al., 2007). For the majority of the examples presented, a weak coupling between the fluid and structural systems was able to capture the dynamics with sufficient accuracy. A strong iterative coupling was employed for the tandem cylinders case presented in Section 3.3, for which $\rho^* = 2.546$. Within this simple iterative approach, we measure the L^∞ norm of the relative difference in the body displacement between two successive iterations and iterate until its value is below the convergence tolerance $tol = 10^{-8}$. The method usually converges within two to six iterations. For the investigated cases, though, the loosely and strongly coupled algorithms yield negligible differences, as shown in fig. 9 of Borazjani and Sotiropoulos (2009) within a similar IB-FSI framework.

The simulations employed for the stability calculations were performed with a fixed time-step taken small enough to keep the CFL condition around the value of 0.2, in order to capture the FSI dynamics with sufficient accuracy for all explored configurations. The average spacing between adjacent Lagrangian markers was set equal to $0.5\Delta x_{loc}$, where Δx_{loc} is the local Eulerian cell dimension. Further details on the method can be found in Nitti et al. (2020).

2.2.1. Immersed boundary procedure

The boundary conditions at the fluid–structure interface are imposed on the provisional velocity field using a direct-forcing immersed boundary technique. Following Uhlmann (2005), body-force terms are computed over a set of suitably spaced Lagrangian markers laying on the immersed surface. Each velocity component is interpolated at the Lagrangian markers via an MLS approximation (Vanella and Balaras, 2009),

$$\hat{V}_i(\mathbf{x}^l) = \mathbf{\Psi}^\mathsf{T}(\mathbf{x}^l)\hat{\mathbf{u}}_i, \tag{10}$$

where $\hat{\mathbf{u}}_i$ is the array that collects the ith velocity component at the face centers within the support domain (see Fig. 1) of each Lagrangian marker and $\hat{V}_i$ is the ith velocity component at the Lagrangian position $\mathbf{x}^l$. In two dimensions, the minimum number of grid cells n_e contained in the support domain is equal to 9. The linear operator $\mathbf{\Psi}^\mathsf{T}(\mathbf{x}^l)$ is defined as

$$\mathbf{\Psi}^\mathsf{T}(\mathbf{x}^l) \equiv \mathbf{p}^\mathsf{T}(\mathbf{x}^l)(\mathbf{A}(\mathbf{x}^l))^{-1}\mathbf{B}(\mathbf{x}^l), \tag{11}$$

where

$$
\begin{aligned}
\mathbf{p}^\mathsf{T}(\mathbf{x}^l) &= [1, x^l, y^l], \\
\mathbf{A}(\mathbf{x}^l) &= \sum_{k=1}^{n_e} W\left(\mathbf{x}^l - \mathbf{x}^k\right) \mathbf{p}\left(\mathbf{x}^k\right) \mathbf{p}^\mathsf{T}\left(\mathbf{x}^k\right), \\
\mathbf{B}(\mathbf{x}^l) &= \left[W(\mathbf{x}^l - \mathbf{x}^1)\mathbf{p}(\mathbf{x}^1) \ldots W(\mathbf{x}^l - \mathbf{x}^{n_e})\mathbf{p}(\mathbf{x}^{n_e})\right].
\end{aligned}
\tag{12}
$$

The weight function $W(\mathbf{x}^l - \mathbf{x}^k)$ plays the role of a convolution kernel. Throughout this work, the exponential function is used,

$$
W(\mathbf{x}^l - \mathbf{x}^k) = \begin{cases} e^{-(r_k/\epsilon)^2} & \text{for } r_k \leq 1 \\ 0 & \text{for } r_k > 1 \end{cases} \tag{13}
$$

where $r_k = |\mathbf{x}^L - \mathbf{x}^k|/r_i$, with r_i the size of the support domain in the ith direction and $\epsilon = 0.3$. A volume force component is then computed for each Lagrangian marker l,

$$F_i^l = \frac{V_i^l - \hat{V}_i(\mathbf{x}^l)}{\Delta t}, \tag{14}$$

where V_i^l is the ith component of velocity to be imposed at the interface and Δt is the time-step of the numerical scheme. Finally, the forcing term to be added to the RHS of the Navier–Stokes equations (1) is computed at each Eulerian grid point using again the shape functions of the interpolation procedure

$$f_i^k = \sum_{l=1}^{n_l} c_l \Psi_k^l F_i^l, \tag{15}$$

where f_i^k is the ith component of the forcing for the kth Eulerian grid point, n_l is the number of Lagrangian markers whose support domain contains the selected Eulerian point and c_l is a scaling coefficient (see Nitti et al. (2020) for details).

2.3. Linear stability

In this section, we focus on the linear stability of the coupled system. After spatial discretization, fluid and solid variables are collected into the state vector $\boldsymbol{q}$, and the problem is reformulated as

$$\frac{d\boldsymbol{q}}{dt} = \boldsymbol{R}(\boldsymbol{q}), \tag{16}$$

where $\boldsymbol{R}$ is the nonlinear evolution operator of the system. The linear stability of a steady-state $\boldsymbol{q}_b$ of the system ($\boldsymbol{R}(\boldsymbol{q}_b) = \boldsymbol{0}$) can be studied by observing the evolution in time of a small-amplitude perturbation, $\epsilon\boldsymbol{q}'$, superimposed on the base state ($\boldsymbol{q}(t) = \boldsymbol{q}_b + \epsilon\boldsymbol{q}'(t)$). By injecting this decomposition into (16) and retaining only the first-order terms, the evolution of $\boldsymbol{q}'$ is governed by

$$\frac{d\boldsymbol{q}'}{dt} = \left.\frac{\partial \boldsymbol{R}}{\partial \boldsymbol{q}}\right|_{\boldsymbol{q}_b} \boldsymbol{q}' = \boldsymbol{J}(\boldsymbol{q}_b)\boldsymbol{q}', \tag{17}$$

where $\boldsymbol{J}(\boldsymbol{q}_b)$ is the linear Jacobian operator evaluated with respect to the steady-state $\boldsymbol{q}_b$. Following the traditional normal-mode approach, the stability characteristics of the system are deduced from the spectrum of the Jacobian operator,

$$\boldsymbol{q}'(t) = \hat{\boldsymbol{q}}e^{\omega t} + \text{c.c.} \tag{18}$$

$$(\boldsymbol{J}(\boldsymbol{q}_b) - \boldsymbol{I}\lambda)\,\hat{\boldsymbol{q}} = 0 \tag{19}$$
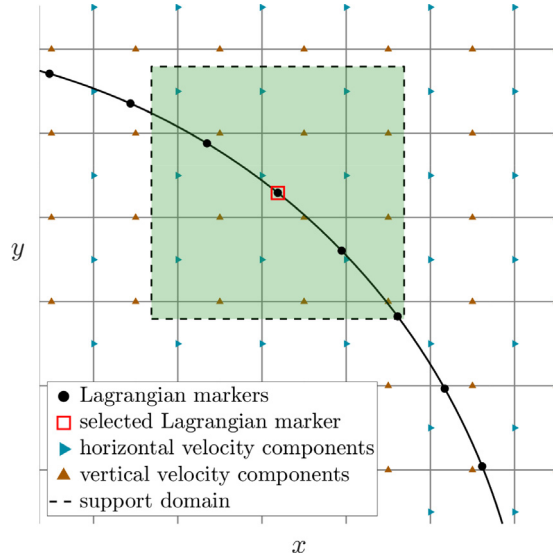
Fig. 1. Scheme of the IB forcing. The Eulerian nodes contained in the support domain of the selected marker are involved in the forcing procedure.

where ω is a complex eigenvalue, $\hat{q}$ is the spatial structure of the related eigenmode and $c.c.$ indicates the complex conjugate. For an autonomous system, the exact solution of the linear initial value problem expressed by Eq. (17) is given by

$$q'(t_0 + T) = e^{J(q_b)T} q'(t_0) = \Phi(T) q'(t_0), \tag{20}$$

where the operator Φ is known as the *exponential propagator* of the system. Injecting into Eq. (20) the modal decomposition, we get the following eigenvalue problem

$$\mu \hat{q} = \Phi(T) \hat{q}. \tag{21}$$

The eigenvalues of the two problems are related through the exponential transformation $\mu = e^{\omega T}$, while the eigenvectors remain unchanged. The asymptotic linear stability properties of the system are dictated by the module of the eigenvalues μ. If all eigenvalues have $|\mu| < 1$, the system is linearly stable, while it is unstable if at least one eigenvalue has $|\mu| > 1$. For $|\mu| = 1$, the system is neutrally stable. The exponential transformation alters the spectrum in such a way that the *dominant* eigenvalues, *i.e.* the eigenvalues of largest modulus, correspond to the leading ones in the original eigenvalue problem, where with the term *leading*, we refer to the eigenvalues with the largest real parts.

2.3.1. Numerical strategy

The problem of linear stability is now reduced to finding the eigenvalues of an $N \times N$ matrix Φ, where the dimension N is given by the number of cells or nodes of the discretized domain times the number of flow variables, plus the degrees of freedom of the body. For real-world systems, the explicit calculation (and storage) of the matrix exponential often carries a prohibitive computational load and one must resort to iterative algorithms, such as those belonging to the class of Krylov-subspace projection methods. In these algorithms, an M-dimensional Hessenberg matrix H (with $M \ll N$) approximates the matrix exponential in a low-dimensional Krylov subspace, which is constructed via the repeated action of operator Φ on a given starting vector. The eigenvalues of the Hessenberg matrix, the so-called *Ritz values*, constitute an approximation of the eigenvalues of the exponential matrix.

Given the matrix-free framework of this method, we aim at the approximation of the action of Φ on a perturbation vector. In doing so, we introduce the propagator $F(q)$ of the complete solution,

$$q(t_0 + T) = F(q_0, T), \tag{22}$$

where $q_0 = q(t = t_0)$ is the value assumed by the state vector q at a given time $t = t_0$ and $q(t_0 + T)$ represents its evolution after a time T. The solution at time $t = t_0$ can be expressed as the superposition of the previously defined steady-state q_b and a small amplitude deviation for this base state $\epsilon q'(t_0)$. A Taylor expansion of operator F around the base state q_b yields

$$F(q_b + \epsilon q'(t_0), T) = F(q_b, T) + \left.\frac{\partial F(q, T)}{\partial q}\right|_{q_b} \epsilon q'(t_0) + O(\epsilon^2), \tag{23}$$

where $\epsilon q'(t_0)$ represents a small deviation from the base state.

It can be shown that the second term on the RHS is, up to the scalar ϵ, an approximation of $(\boldsymbol{q}'(t_0 + T) - \boldsymbol{q}'(t_0))$ for small values of T. The details of this derivation are provided in Appendix A.

Substituting the derivative of $\boldsymbol{F}(\boldsymbol{q}, T)$ into the RHS of (23) and neglecting higher order terms in ϵ, we get an expression for evaluating the advancement in time of the perturbation based only on the propagator of the complete solution,

$$\boldsymbol{q}'(t_0 + T) \approx \frac{\boldsymbol{F}(\boldsymbol{q}_b + \epsilon\boldsymbol{q}'(t_0), T) - \boldsymbol{F}(\boldsymbol{q}_b, T)}{\epsilon}. \tag{24}$$

Taking the limit of Eq. (24) as $\epsilon \to 0$, the RHS gives a Gateaux derivative of $\boldsymbol{F}$ at $\boldsymbol{q}_b$,

$$\lim_{\epsilon \to 0} \frac{\boldsymbol{F}(\boldsymbol{q}_b + \epsilon\boldsymbol{q}'(t_0), T) - \boldsymbol{F}(\boldsymbol{q}_b, T)}{\epsilon}. \tag{25}$$

In a discrete context, the action of the time-marching matrix of the perturbation can be recovered through a finite difference that only involves calls to the time-stepping scheme described in Section 2.2 (here we have adopted the same nomenclature to refer to both discrete and time-continuous operators). Selecting a small but non-zero value of ϵ, the derivative given by (25) can be approximated by

$$\frac{\boldsymbol{F}(\boldsymbol{q}_b + \epsilon\boldsymbol{q}_p(t_0), n\Delta t) - \boldsymbol{F}(\boldsymbol{q}_b, n\Delta t)}{\epsilon}, \tag{26}$$

where $\boldsymbol{q}_p$ represents the perturbation vector in the discrete system. For ease of notation, we employ the same notation $\boldsymbol{q}_b$ to refer to both the continuous and discrete base state. The parameter n is the number of time-steps by which the solution is advanced in time and Δt is simply the time-step of the scheme, chosen according to the desired *CFL* condition.

A better approximation of (25) can be built via higher-order finite differences. In the present work, we employ a second-order finite difference to approximate the evolution of a given perturbation $\boldsymbol{q}_p(t_0)$:

$$\boldsymbol{q}_p(t_0 + n\Delta t) = \frac{\boldsymbol{q}_+ - \boldsymbol{q}_-}{2\epsilon}, \tag{27}$$

where $\boldsymbol{q}_+$ and $\boldsymbol{q}_-$ are the results of two separate calls to the FSI solver, advancing in time the base state after the addition and subtraction, respectively, of the same small perturbation:

$$\boldsymbol{q}_+ = \boldsymbol{F}(\boldsymbol{q}_b + \epsilon\boldsymbol{q}_p(t_0), n\Delta t), \tag{28}$$

$$\boldsymbol{q}_- = \boldsymbol{F}(\boldsymbol{q}_b - \epsilon\boldsymbol{q}_p(t_0), n\Delta t). \tag{29}$$

Although such an approach presents the disadvantage of requiring two calls to the time-stepper, it reduces the number of required iterations by providing a more accurate estimate for the matrix–vector product (Knoll and Keyes, 2004).

We can compute a set of the least stable eigenvalues via a Krylov projection method. In this work, approximations to the leading eigenvalues of the system are computed using the *implicitly restarted Arnoldi method* (IRAM) (Sorensen, 1992) as implemented in the ARPACK open source package (Lehoucq et al., 1998).

The base states here considered are equilibrium solutions of the fully coupled nonlinear system, therefore their evaluation requires the solution of a nonlinear algebraic system.

For large-scale problems, a pure Newton–Raphson method is prohibitive because of the size of the systems, hence the most common approach to overcome this difficulty is the use of a Newton–Krylov technique. In this work, the base state for each test case was computed using *BoostConv* (Citro et al., 2017), an iterative residual recombination procedure belonging to the class of Krylov methods.

The choice of such an algorithm fits perfectly into our matrix-free approach since *BoostConv* can be easily applied as a black-box procedure requiring only several calls to a pre-existing time-marching algorithm, without any modification.

The outline of the algorithm is shown below:

1. The base flow is computed via *BoostConv* (Citro et al., 2017)
2. Arnoldi iterations are performed until the desired convergence is reached: $(k = 1, 2, \ldots)$

    (a) Vector $\boldsymbol{q}_p^k$ is generated
    (b) Reverse communication (Lehoucq et al., 1998) with the flow solver provides $\boldsymbol{q}_p^k = \frac{\boldsymbol{q}^+ - \boldsymbol{q}^-}{2\epsilon}$
    (c) Convergence of the desired Ritz pairs is checked

3. A logarithmic transformation is performed to recover the original eigenvalues: $\lambda = (\log|\mu| + i\arg(\mu))(n\Delta t)^{-1}$.

For all cases shown in this article, a non-zero pseudo-random perturbation has been employed as a starting vector for the Arnoldi iterations, respecting the divergence constraint on the velocity. It is worth pointing out that the present approach circumvents the need to select appropriate boundary conditions for the perturbation field, while the boundary conditions of the nonlinear evolution problem are included in the discrete operator $\boldsymbol{F}$.

Some remarks on the effect of the IB interface on the linear results. With the IB approach, the solid–fluid interface is enforced by a time-varying distribution of forcing terms that mimics the effect of the body on the flow. Since, in general, the interface does not coincide with the grid lines, the need for an interpolation procedure arises. The way this transfer of information is done defines the specific variant of the IB method.

In the presence of a moving interface, the choice of the interpolation scheme is even more important. It has been noted, for instance, that non-physical force oscillations arise, in this case, with some variants of the IB method (Yang et al., 2009), like the discrete Delta function formulation. Complications emerge also with the Cartesian grid (or cut-cell) approach, in which the fluid–solid interface is sharply tracked, in view of the fact that the role of the grid points near the interface can change from time-step to time-step (Yang and Balaras, 2006) (*i.e.* a grid point that belongs to the portion of the domain occupied by the solid at a given time-step can drop out of the body contour at the next time-step and viceversa). While the role of the node changes, it still carries the physical information about its previous phase, consequently, the local pressure field is strongly perturbed.

The choice of the above-described MLS technique, among the diverse options belonging to the class of non-conforming methods, is motivated by the need for a smooth transfer between Lagrangian and Eulerian nodes (Vanella and Balaras, 2009; Uhlmann, 2003). Indeed, the emergence of non-physical pressure oscillations in the nonlinear solution would have a detrimental impact on the accuracy of Eq. (27), involved in the computation of the linear modes with respect to the steady-state. The present method shows reduced spurious oscillations in the vicinity of the interface due to the fact that the IB forcing field is slightly smeared within the compact support of the MLS interpolation.

One issue of interest is to what extent the smeared representation of the interface affects the accuracy of the computation for higher Reynolds number flows. The wall-resolved computation of the viscous shear layer in presence of moving immersed boundaries is still an open research area. One way to improve the local accuracy with reasonable computational expense within an IB framework is to employ a locally refined semi-structured grid (Durbin and Iaccarino, 2002; de Tullio et al., 2007) in order to increase the grid resolution near the body. It is worth recalling that the present method relies on the linearization of the system around steady solutions of the Navier–Stokes equations, which usually exist for sufficiently low Reynolds numbers.

Another point to be considered is the effect of the IB treatment on the evaluation of the finite difference in Eq. (27) itself. When the position of a given Lagrangian marker falls into a certain grid cell in the solution $\boldsymbol{q}_+$ and into an adjacent cell in $\boldsymbol{q}_-$, the subtraction $(\boldsymbol{q}_+ - \boldsymbol{q}_-)$ involves grid points that are included in the support domain of the marker in one case and left out in the other. To avoid this problem, the support domain of each marker is kept fixed during the evaluation of $\boldsymbol{q}_+$ and $\boldsymbol{q}_-$, such that the forced fluid cells are the same in the two solutions. The corresponding marker is prevented from falling outside of the fixed support owing to the short integration time T and the small scaling factor ϵ employed in the linearization procedure. In this way, the procedure provides an accurate and robust computation of leading modes with a finite difference approach.

2.3.2. Selection of the linearization parameters

One critical aspect of the presented procedure is the selection of the linearization parameters, *i.e.*, the integration period $T = n\Delta t$ and the perturbation scaling factor ϵ.

The choice of the integration time is somewhat problem dependent. As reported by Goldhirsch et al. (1987), for a given number of requested eigenvalues k, the order of the error related to the model reduction is given by $|e^{(\lambda_k - \lambda_M)T}|$. This means that the accuracy can be improved either by increasing the number of integration time steps n, or by augmenting the dimension of the basis M. Eriksson and Rizzi (1985) refer to n as a *selectivity* parameter, in the sense that, as it increases, the separation among the least damped eigenvalues is magnified. Both options can provide sufficient separation between the desired eigenvalues and the remaining part of the spectrum.

In spite of that, it is worth noting that this methodology is based on an approximation of the evolved perturbation, given by Eq. (24), which is valid for short integration periods. For this reason, it is legitimate to keep T small while increasing the value of M for particularly clustered eigenvalues.

One issue to be considered when dealing with iterative methods is the need for convergence acceleration that arises for high-resolution simulations. The rate of convergence of an iterative method decreases with the condition number of the Jacobian matrix, which in turn increases as the grid is refined. To address this issue and improve the performance of the method, adequate preconditioning is usually required. Building a preconditioner in a matrix-free context is not a trivial task because the matrix is never formed and standard preconditioning techniques cannot be directly applied.

To preserve the flexibility of the time-stepping global stability solver, the technique employed to control the convergence must be iterative and matrix-free. As an example, Mack and Schmid (2010) proposed a Jacobian-free DNS-based global stability solver for compressible flows with the addition of a preconditioning matrix in explicit form. Instead, Asgharzadeh and Borazjani (2017) addressed this issue through the use of an analytical Jacobian as a preconditioner in a Newton–Krylov method for the implicit solution of the Navier–Stokes equations. Some other options for matrix-free preconditioning are discussed in Knoll and Keyes (2004).

The remaining parameter that must be selected by the user is the linearization coefficient ϵ, *i.e.* the amplitude of the discrete perturbation. Its value should result from a trade-off between the truncation error of the finite difference and round-off errors related to the finite precision arithmetic.
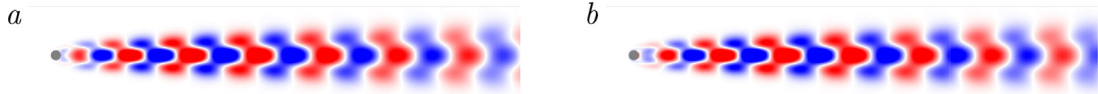
Fig. 2. Spatial distribution of the vorticity for the real (a) and imaginary (b) parts of the unstable eigenmode of the flow past a fixed circular cylinder at $Re = 50$.

Table 1
Unstable eigenvalue for the flow past a fixed circular cylinder at $Re = 50$. Present results show good agreement with values present in the literature, as indicated by the relative error reported on the right.

Reference	ω	(%)
Siconolfi et al. (2017)	$0.0160 + 0.759i$	2.85
Negi et al. (2020)	$0.0133 + 0.742i$	0.61
Present	$0.0154 + 0.738i$	–

Literature provides some guidelines for the appropriate choice of ϵ, the interested reader is referred to the works of Eriksson and Rizzi (1985), Knoll and Keyes (2004), Schulze et al. (2009) and Mack and Schmid (2010). In this work, we follow a commonly used approach that selects the scaling factor of the perturbation at each time-stepper call via

$$\epsilon = \epsilon_0 \frac{\|\boldsymbol{q}_b\| + \|\boldsymbol{q}_p\|}{\|\boldsymbol{q}_p\|}, \tag{30}$$

where $\|\boldsymbol{q}\|$ is the L_2 norm of vector $\boldsymbol{q}$ and ϵ_0 is a user-defined parameter related to the truncation error (An et al., 2011) of the FSI time-stepping scheme.

The choice of ϵ_0 has a great influence on the success of this time-stepping approach, and the user should keep in mind that this task is somewhat solver-dependent. Following the example of Mack and Schmid (2010), we report in Appendix C a parametric study that illustrates the influence of the parameter ϵ_0 on the accuracy of the results obtained for a given configuration.

3. Validation and results

In this section, to validate the algorithm derived above, we present the results of several numerical tests involving the vortex-induced vibration (VIV) of elastically mounted circular cylinders in a cross-flow. After the validation, a multi-body configuration is finally explored, consisting of the VIV of two identical spring-mounted cylinders in tandem configuration.

3.1. Flow past a fixed circular cylinder

The proposed methodology has been first validated with respect to the two-dimensional flow past a fixed circular cylinder, which is the subject of abundant literature in the field of hydrodynamic instability as it is considered the prototype flow around bluff bodies.

For this case, the flow quantities are made dimensionless by taking the diameter of the cylinder D and the incoming flow velocity U_∞ as reference variables. The reported results are obtained over a rectangular domain with size $[-28D : 52D] \times [-28D : 28D]$, with the origin placed on the cylinder axis. A uniform streamwise velocity is imposed at the inlet boundary along with a zero cross-sectional velocity ($u = 1$, $v = 0$), while free-shear boundary conditions are enforced on the lateral boundaries. At the outlet, a convective boundary condition allows the outgoing waves to exit the computational domain with minimal reflections while preserving local continuity. No-slip conditions are applied to the velocity at the surface of the cylinder via the IB procedure described in the previous section. Fig. 3 illustrates an example of the stretched Cartesian grid used for the computations. To obtain the results here presented, a grid containing 900×570 cells was employed, with a minimum grid spacing of $0.022D$ attained over a uniformly spaced rectangular region around the cylinder measuring $10D$ in the streamwise direction and $4D$ in the cross-stream direction.

An estimate for the globally unstable eigenvalue ω at $Re = 50$ is reported in Table 1 along with results from Refs. Siconolfi et al. (2017) and Negi et al. (2020), while Fig. 2 shows the vorticity field of the real and imaginary parts of the related unstable eigenmode.

3.2. VIV of an isolated cylinder

As a second validation case, we report the results of the linear stability analysis of the VIV of an isolated elastically mounted circular cylinder, to test the ability of our IB solver to accurately capture the dynamics of a small perturbation of the fluid–structure system.
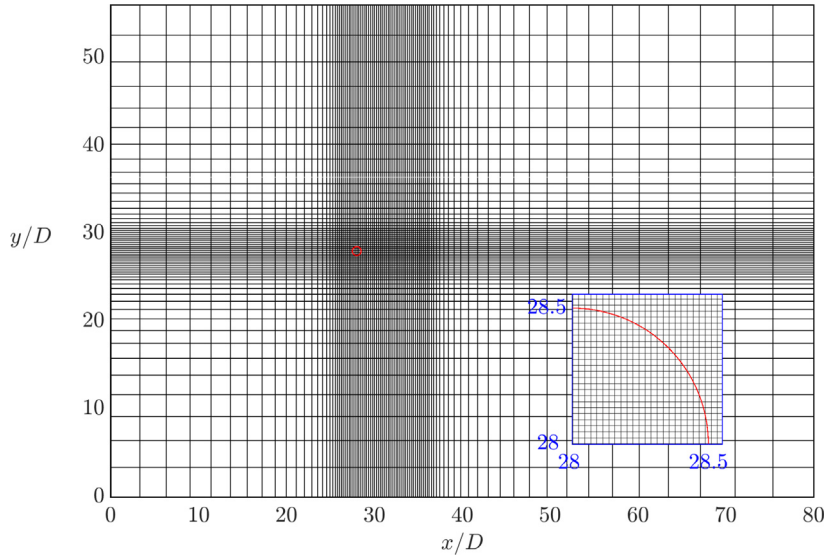
Fig. 3. Example of a grid used for the linear stability analysis of the flow past a circular cylinder (for both the fixed and oscillating cases). To make the graph more readable, every tenth grid point in each direction is displayed. The inset shows a close-up of the cylinder region for the actual grid employed in the calculations.

The size of the domain and the distance of the center of mass of the cylinder from its boundaries are the same as in the case of the fixed cylinder, as well as the boundary conditions. For all cases investigated, the Reynolds number based on the cylinder diameter is kept fixed at $Re = 60$, the cylinder being free to oscillate only in the cross-stream direction with no structural damping.

For the computations, the same grid used for the case of the fixed cylinder was employed after a grid convergence study. Results and details of the grid refinement study are reported in Appendix B together with an investigation of the influence of the domain size on the accuracy of the results.

In Fig. 4, we report the variation of the non-dimensional frequency and growth rate of the two least stable eigenvalues with the reduced velocity U^*, for two distinct values of the relative density, namely, $\rho^* = 20$ and $\rho^* = 5$. For the largest density ratio, the two leading modes exhibit a clear distinction for each value of the reduced velocity U^*. Following Navrose and Mittal (2016), we denote them as the *fluid mode* (FM), due to the high affinity that it shows with the wake mode of the fixed cylinder (see Fig. 5), and the *elastic mode* (EM). This classification is further confirmed by noticing how the frequency of the FM remains close to that of the unstable mode for the flow around a fixed cylinder at the same Reynolds number (see Table 1) for all values of U^*, while the frequency of the EM, on the other hand, decreases following the variation of the natural frequency of the cylinder, given by $1/U^*$.

For $\rho^* = 5$, the two modes lose their distinction for intermediate values of U^*, therefore, following Navrose and Mittal (2016), we refer to them as the coupled fluid–elastic modes (FEM) I and II. For low values of U^*, modes *FEMI* and *FEMII* resemble the stationary wake mode (*i.e.* the mode associated with the vortex-shedding in the wake of the fixed cylinder) and the elastic mode, respectively; however, as U^* increases, the two eigenmodes become coupled and exchange their characteristics (see Fig. 6).

3.3. Flow-induced vibrations of two cylinders in tandem

The case considered in this section is the configuration proposed by Borazjani and Sotiropoulos (2009), with two identical elastically mounted cylinders in tandem arrangement placed in a free-stream flow. A parametric exploration of the dynamics of the system is beyond the scope of the current work, so we restricted our analysis to the 1-DOF case in which the cylinders are free to oscillate only in the cross-stream direction. The streamwise distance between their centers is equal to 1.5 diameters, while the cross-stream offset is zero. No structural damping is considered and the solid-to-fluid density ratio is kept constant at $\rho^* = 2.546$ for all simulations. Given the low value of the density ratio and the close proximity of the cylinders, the problem under investigation represents a challenging test case that can prove the flexibility of the method.

We first present the nonlinear response of the cylinders at the diameter-based Reynolds number $Re = 200$, for values of the reduced velocity spanning the range $1.5 \le U^* \le 14$. A sketch of the computational domain along with the boundary conditions employed is shown in Fig. 7. The inlet is located at a distance $L_{in} = 15D$ from the midpoint between the centers of the cylinders, with the total length of the domain being equal to $L_{in} + L_{out} = 55D$, while the lateral boundaries are placed
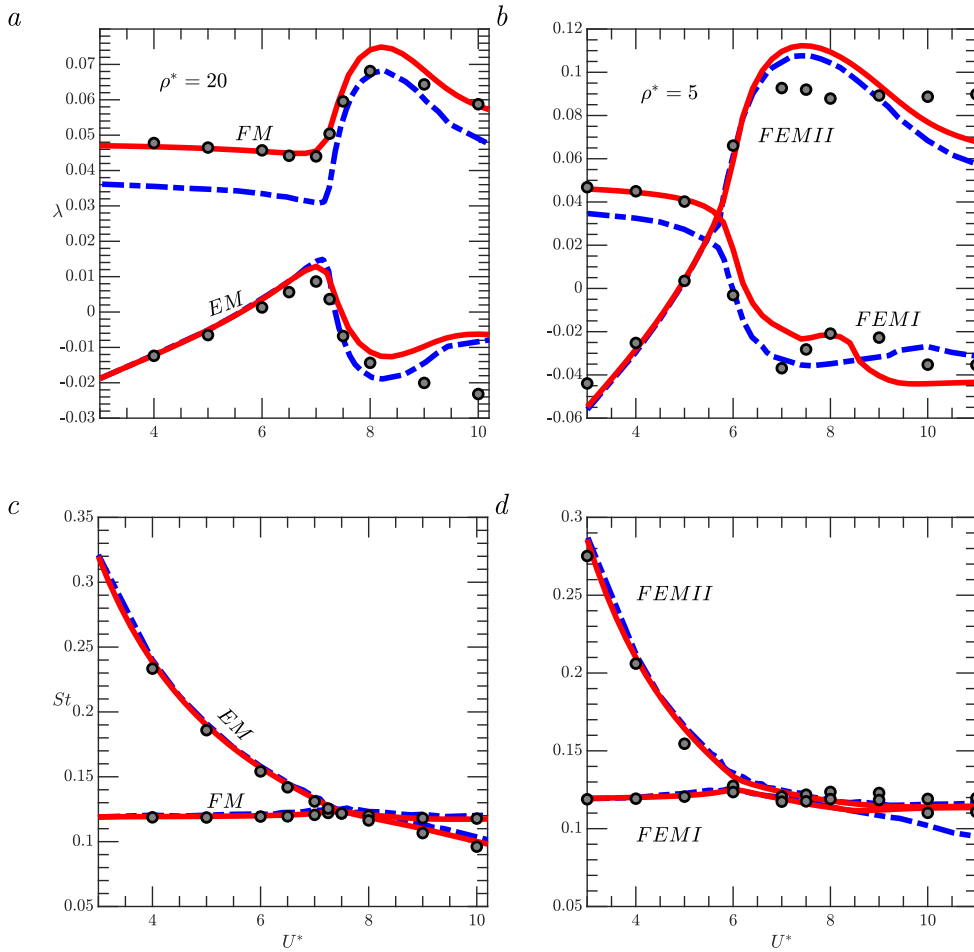
Fig. 4. Linear stability results: change of the growth rate λ and the Strouhal number, $St = (fD)/U_\infty$, of the two least stable modes with U^* for $\rho^* = 20$ (a, c) and $\rho^* = 5$ (b, d) at $Re = 60$. Continuous red line: results from Sabino et al. (2020); dashed blue line: results from Navrose and Mittal (2016); gray circles: present results. The red curves were reproduced using the open-source Matlab drivers of the StabFem project (https://gitlab.com/stabfem/StabFem). (For interpretation of the references to color in this figure legend, the reader is referred to the web version of this article.)
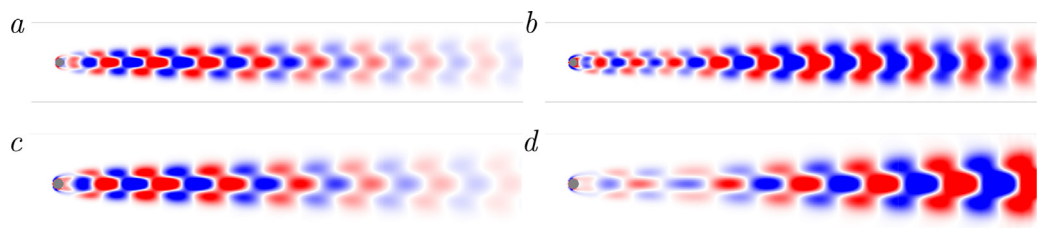
Fig. 5. Spanwise vorticity field of the real part of FM (a, c) and EM (b, d) for ($Re = 60$, $\rho^* = 20$) at $U^* = 7$ (a, b) and $U^* = 9$ (c, d). The fluid flows from left to right. Note how the fluid mode resembles the unstable mode for a fixed cylinder reported in Fig. 2.

at a distance $L_{lat} = 15D$ from the centers. A uniform Dirichlet boundary condition is given at the inlet and on the lateral boundaries, while a convective condition is assigned at the outlet with a convective velocity $c = 0.8$. The computations were performed over a stretched Cartesian grid containing 900×520 cells, with a minimum grid spacing of $0.0154D$ in the regularly spaced box region around the origin, measuring $4D$ in each direction.

All simulations were initialized with the steady base flow computed via *BoostConv* (Citro et al., 2017) by keeping the cylinders fixed at their initial positions. No starting perturbation was superposed to the stabilized solution; thus, the initial departure from the base flow was triggered only by round-off errors. Fig. 8 shows the temporal evolution of the
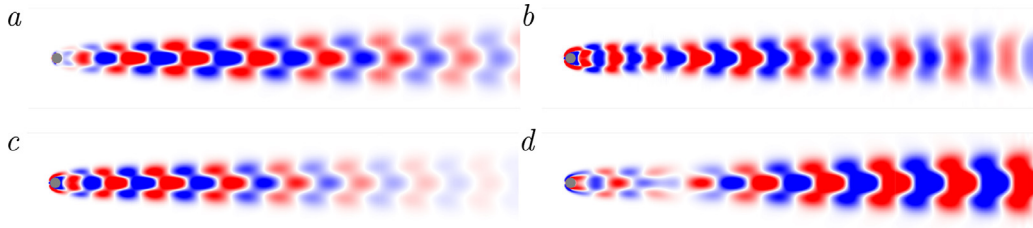
Fig. 6. Spanwise vorticity field of the real part of FEMI (*a*, *c*) and FEMII (*b*, *d*) for ($Re = 60$, $\rho^* = 5$) at $U^* = 5$ (*a*, *b*) and $U^* = 6$ (*c*, *d*). The fluid flows from left to right.
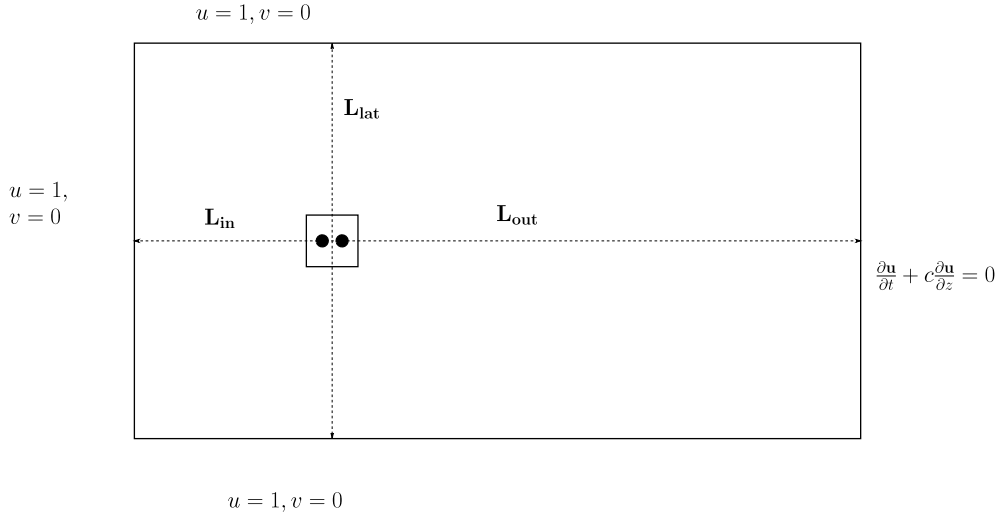

Fig. 7. Sketch of the computational domain employed for the direct numerical simulations of the flow interacting with two circular cylinders in tandem arrangement at $Re = 200$.

position of the centers of mass of the two cylinders for different values of U^*, each one being representative of a distinct behavior of the system. For $U^* = 3$ (see Fig. 8(a)) the cylinders experience a longer transient phase characterized by low-amplitude vibrations before reaching a periodic regime where the two cylinders oscillate out-of-phase with the front one exhibiting higher amplitude than the rear. Borazjani and Sotiropoulos (2009) classified this behavior as state 1 of the system and referred to the vibration state where the rear cylinder achieves a larger oscillation amplitude as state 2. When the reduced velocity is increased to $U^* = 4$, the dynamic response of the fluid–structure system changes noticeably as the two cylinders exhibit a quasi-periodic behavior distinguished by larger amplitudes of vibration that undergo a low-frequency modulation in time. As can be seen from the close-up region in Fig. 8(b), such modulations come with a change in the phase difference between the two oscillatory motions, as the phase angles are generally out of phase, but match periodically.

As the reduced velocity is further increased to $U^* = 5$, a shift from state 1 to state 2 is observed and the two cylinders oscillate in phase opposition, with the rear one exhibiting greater amplitude than the front one. For higher values of the reduced velocity, there is no qualitative change in the dynamical response of the system. The trailing cylinder continues to oscillate at a higher amplitude and out-of-phase with respect to the front one. Fig. 9(a) shows the variation of the maximum displacement A^*_{MAX} with the reduced velocity for each cylinder; the A^*_{MAX} value was measured disregarding the early transient phase. Results from Borazjani and Sotiropoulos (2009) and Griffith et al. (2017) are also included for comparison, showing a good overall agreement with the present outcome. The main discrepancy observed for the higher values of U^* can be ascribed to the different initial conditions. To verify this assumption, we repeated the computations for $11 \leq U^* \leq 14$ starting from a snapshot of the unsteady solution at $U^* = 10$; the results, represented in Fig. 9(a) by dashed lines, are markedly closer to the data present in the literature. These findings could indicate the existence of a hysteresis effect, already observed for the case of two stationary cylinders in tandem (Papaioannou et al., 2006) and for the VIV of a single cylinder (Prasanth and Mittal, 2009; Singh and Mittal, 2005). However, a detailed characterization of the system dynamics is beyond the scope of this article. Results obtained by running simulations of the same configuration at $Re = 100$ are presented in Fig. 9(b); the behavior of the system is found to depend strongly on the reduced velocity with a good qualitative agreement with the $Re = 200$ case. Time traces of the displacements of the two cylinders are reported in Fig. 10 for four different values of the reduced velocity, along with the spectral content of the time history of
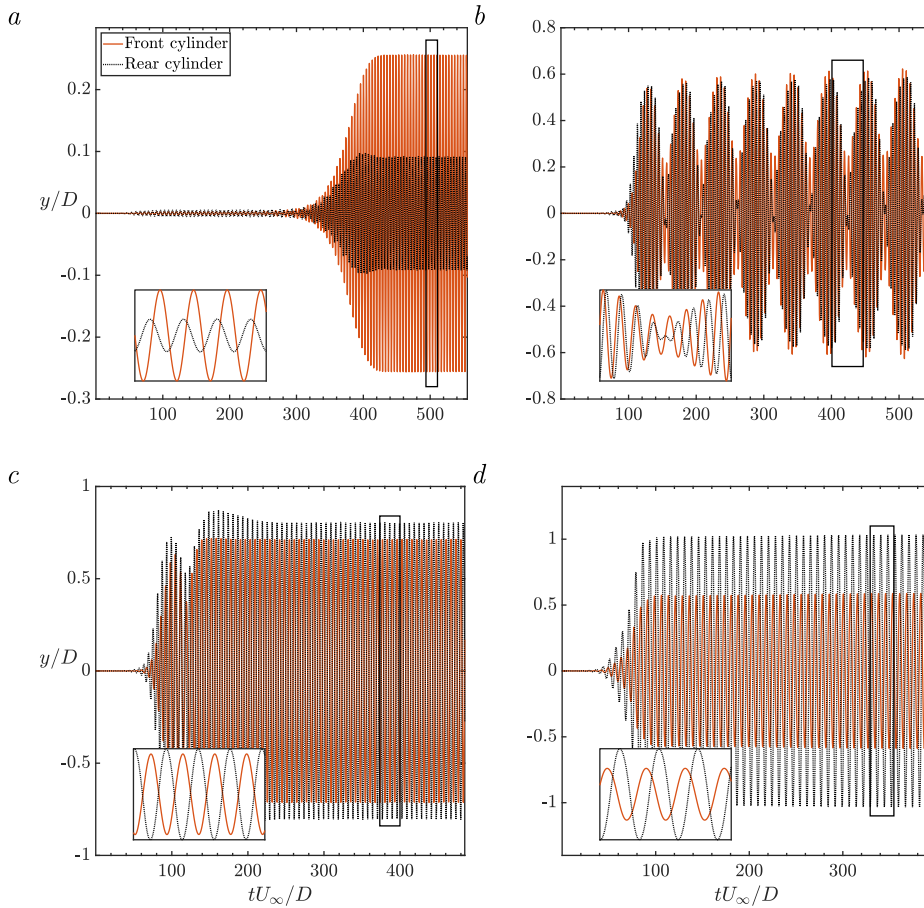
Fig. 8. Flow past two freely vibrating cylinders in tandem at $(Re, \rho^*) = (200, 2.546)$: time evolution of the vertical displacement of the cylinders for different values of U^*; *a*: $U^* = 3$; *b*: $U^* = 4$; *c*: $U^* = 5$; *d*: $U^* = 7$. The inset in the lower-left corner of each figure provides a zoom-in of the region delimited by the black rectangle.

the vertical separation Δy between the centers of the two cylinders. For low values of the reduced velocity, the cylinders are found to oscillate in phase with small amplitudes, indicating that we are still outside the lock-in regime. For $U^* = 3$ (see Fig. 10a), the phase difference between the front and rear cylinders is small, with the rear one exhibiting somewhat larger displacements. When the reduced velocity is increased to $U^* = 4$, the dynamic response of the system changes considerably as the cylinders enter the lock-in regime, oscillating out-of-phase at a higher frequency and with the front cylinder now exhibiting wider oscillations. As the velocity is further increased to $U^* = 5$, a change in the behavior of the system is observed again since the rear cylinder now oscillates with larger relative amplitude, while the vertical separation between the cylinders undergoes oscillations with a periodic amplitude modulation that closely resembles a beating motion. This observation is confirmed by looking at the frequency content in Fig. 10c, which shows two main peaks having similar frequencies. In a linear system, the superposition of these two harmonics would result in a beating frequency, given by $f_b = |f_2 - f_1|$, and a corresponding period of about 97 time units, which is very close to the characterizing period of the oscillations of both cylinders. This beating phenomenon disappears by further increasing the reduced velocity as the frequency of vibration diminishes. It is interesting to notice that Borazjani & Sotiropoulos identified $U^* = 5$ as the critical state of the system at $Re = 200$, delimiting the transition from state 1 to state 2.

3.3.1. Global stability

In this section, we investigate the interaction between the fluid and the two elastically mounted cylinders in tandem through a global linear stability analysis, to further ascertain the validity and robustness of the proposed methodology.

The computations were performed on the same grid used to conduct the flow analysis presented in the previous section. Given the low value of the density ratio ρ^*, the results of the nonlinear simulations obtained with a weak coupling of the fluid and solid dynamics were compared with those obtained via a strong coupling. Even though the two procedures exhibited very similar results, the iterative procedure provided more accurate results with a reduced number of Arnoldi
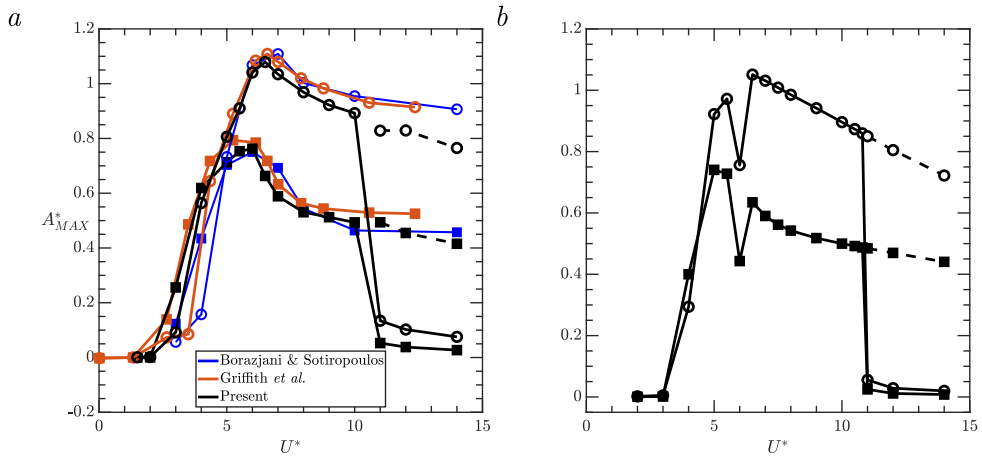
Fig. 9. Variation with the reduced velocity U^* of the maximum non-dimensional displacement A^*_{MAX} of two identical cylinders in tandem ($L = 1.5$) at $Re = 200$ (a) and $Re = 100$ (b). Squares: front cylinder; circles: rear cylinder. The present results for $Re = 200$ are compared with the ones from Borazjani and Sotiropoulos (2009) and Griffith et al. (2017). Dotted line: the simulations were initialized from an instantaneous snapshot of the solution for a smaller value of U^*.
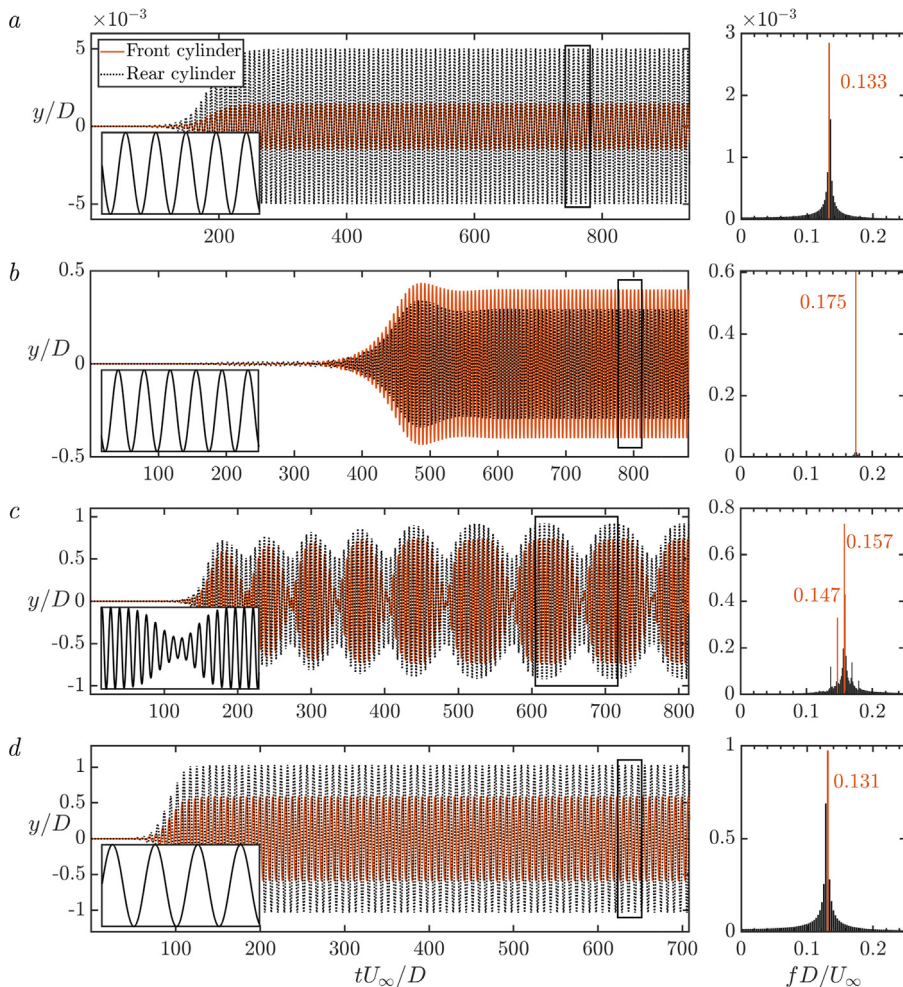

Fig. 10. Flow past two freely vibrating cylinders in tandem arrangement at $(Re, \rho^*) = (100, 2.546)$: time evolution of the vertical displacement of the cylinders for different values of U^*; a: $U^* = 3$; b: $U^* = 4$; c: $U^* = 5$; d: $U^* = 7$. The inset in the lower-left corner of each figure shows the time history of the vertical distance Δy between the cylinders for the time interval marked by the black rectangle. On the right, it is reported the single-sided amplitude spectrum of Δy.
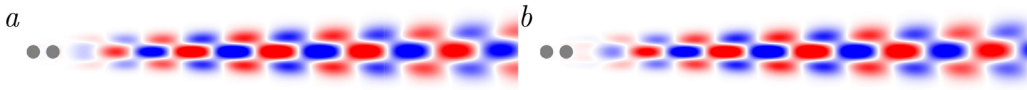
Fig. 11. Spatial distribution of the vorticity for the real (a) and imaginary (b) parts of the unstable eigenmode for the flow past two fixed cylinders in tandem arrangement at $Re = 100$.

iterations for the stability calculations. The fixed time-step size was chosen in order to keep the CFL number under the 0.4 value.

As in the case of the single cylinder, the linear stability analysis of the fluid alone predicts the existence of an unstable eigenvalue $\omega_s = 0.0404 + 0.7907i$ associated with the vortex shedding in the wake of the two cylinders. In the following, we refer to this eigenvalue as the *stationary wake mode*. The corresponding eigenmode (see Fig. 11) closely resembles the unstable eigenmode of the single cylinder case. This observation is consistent with results from literature asserting that, for small streamwise spacings, the two cylinders shed like a single body (Papaioannou et al., 2006).

When the cylinders are free to move in the cross-stream direction, the LSA identifies the presence of an additional eigenmode for the range of parameters considered. In Fig. 12, the two least stable eigenvalues are tracked over a wide range of reduced velocities, in an attempt to identify the mechanisms responsible for the lock-in regime and for the change of behavior that occurs around $U^* = 5$. It is observed that, for the lower values of U^*, the two leading modes are quite distinct, with the frequency of the first mode (represented by blue dots in Figs. 12(b) and 12(d)) being close to the frequency of the stationary wake mode, $f_s D/U_\infty = 0.1258$. Conversely, the frequency associated with the second mode (red dots in Figs. 12(b) and 12(d)) is slightly smaller than the natural frequency of the cylinders for values of the reduced velocity up to $U^* = 7$, where the frequencies of the two modes are almost coincident and remarkably close to that of the limit cycle shown in Fig. 10(d). Therefore, for the lower values of U^*, we associate the first mode with the wake instability and the second one with the structural mode. For $U^* = 5$ the two modes show comparable growth rates and close frequencies, flagging an interaction that is visible in the nonlinear evolution as well. The peak frequencies revealed by the amplitude spectrum on the right side of Fig. 10(c) are, indeed, quite close to the frequencies of the leading modes at $U^* = 5$ reported in Fig. 12(d). After the crossing of the two modes, both frequencies remain close to that of the stationary wake mode for all U^*, and a classification of the modes as fluid mode and structural mode is not possible.

For values of the reduced velocity lower than $U^* = 4$, the mode associated with the structure is still stable. This finding is coherent with the small amplitude of oscillation observed in the calculations. Then, at the critical value $U^* = 5$, the growth rate of mode 2 surpasses that of mode 1, possibly explaining the transition from state 1 to state 2 and the greater amplitudes of vibration observed in the nonlinear simulations. In an attempt to shed further light on this phenomenon, we report in Figs. 12(a) and 12(c) the growth rate and the frequency, respectively, of the two least stable modes for the same tandem arrangement when only the rear cylinder is free to move. For this configuration, we find that the growth rate of the unstable mode increases considerably for $U^* \geq 5$, while the growth rate of the stable mode attains its maximum value.

These results indicate that the mechanism responsible for the large amplitude oscillations is already present in this fixed-free case. The temporal evolution of the flow starting from the base state shows that, for all the values of the reduced velocity, a regular vortex street excites the oscillation of both cylinders, with the rear one undergoing larger vibrations. This is due to the fact that vortices are initially shed only from the rear cylinder, which thus experiences a greater pressure difference. The outcome is coherent with the observations of Borazjani and Sotiropoulos (2009), who suggest that it is the vortex-shedding in the wake that initiates the excitation of the system and subsequently generates a vertical separation between the cylinders. When this separation becomes large enough, other interaction mechanisms come into play and give rise to different dynamical states.

There is, however, another point to address which is the passage from state 2 to state 1 that is observed when changing the value of U^* from $U^* = 3$ to $U^* = 4$ and the switch from state 1 to state 2 that occurs at $U^* = 5$. To investigate this phenomenon, we have reported in Fig. 13a the early transient of the time history of the vertical displacement of the cylinders for $U^* = 4$. It is clearly visible that the cylinders oscillate almost in phase, with a low amplitude of vibration as in the case $U^* = 3$ (Fig. 13b) and the rear cylinder exhibits larger oscillations, following the characteristics of the first mode. The temporal evolution shows that the growth of the first mode saturates as the oscillations approach a limit cycle with small amplitude. Later, the cylinders lose their synchronization owing to the emergence of the second mode. The greater amplitude of vibration of the front cylinder, however, cannot be explained with linear arguments. For $U^* > 5$, the dynamics of the linearized system is governed by the second mode, characterized by the counter-phase oscillation of the cylinders, with the rear one undergoing larger vibrations.

Fig. 14 shows the vorticity fields of the two unstable eigenmodes related to the eigenvalues reported in Fig. 12, for three different values of the reduced velocity. Again, for $U^* = 4$, mode 1 resembles the stationary wake mode of Fig. 11 but departs from it for the higher values of U^*. On the other hand, the shape of mode 2 also changes when the reduced velocity is increased from $U^* = 4$ to $U^* = 5$, while a further increase in the value of U^* produces a shift upstream of the high vorticity region.
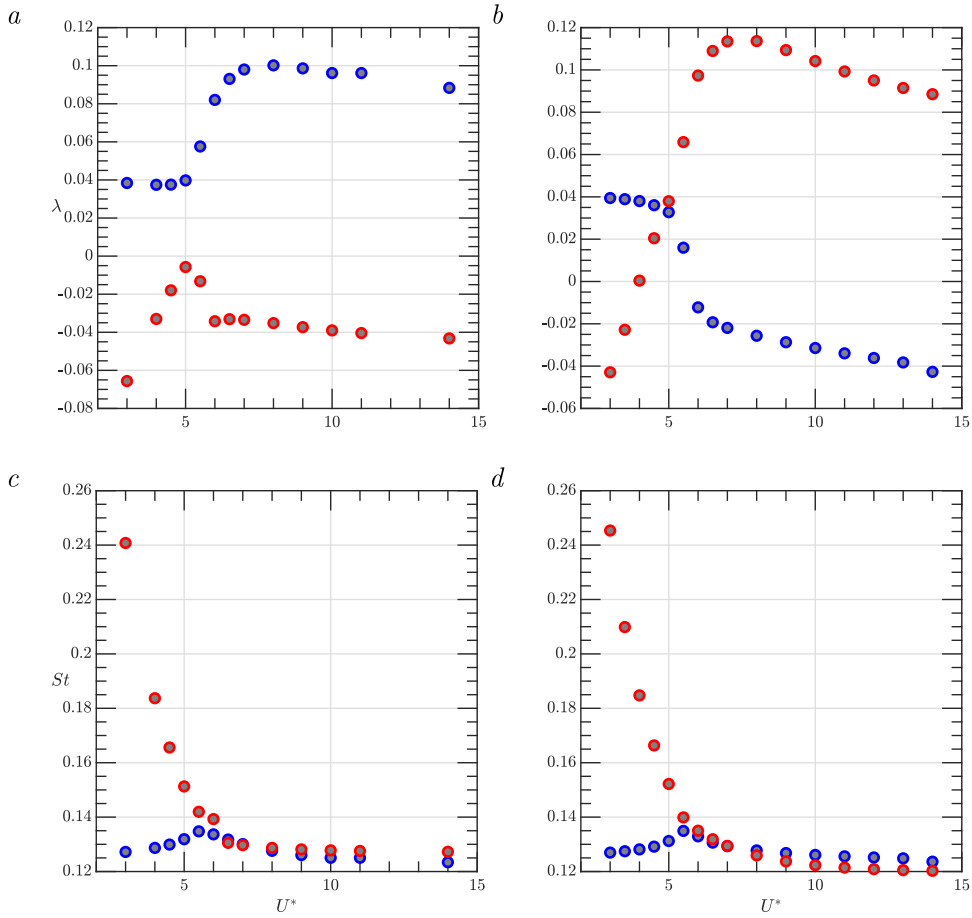
Fig. 12. Results of the LSA for the flow around two elastically-mounted cylinders in tandem at $Re = 100$. Evolution with U^* of the growth rate λ and the Strouhal number St of the two least stable modes. Fig. (a, c): only the rear cylinder is free to oscillate; fig. (b, d): both cylinders are free to move. (For interpretation of the references to color in this figure legend, the reader is referred to the web version of this article.)
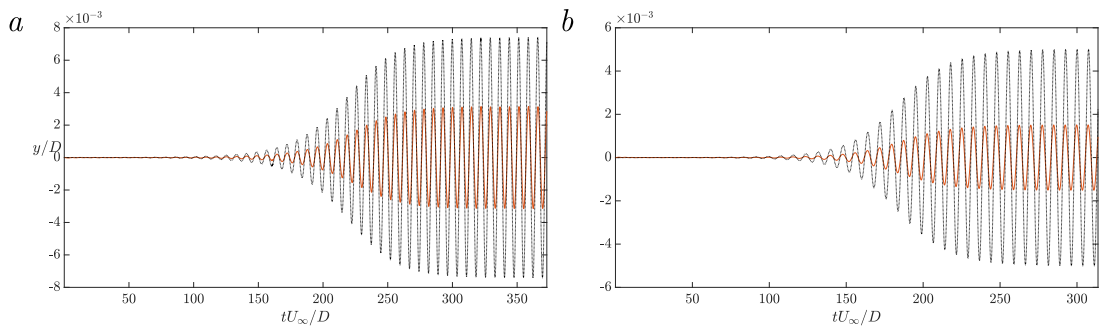

Fig. 13. Time evolution of the vertical displacement of two freely vibrating cylinders in tandem arrangement at $(Re, \rho^*) = (100, 2.546)$ for $U^* = 4$ (a) and $U^* = 3$ (b).

4. Summary and conclusions

The role played by linear effects in the loss of stability of a fluid–structure system has motivated researchers to develop new techniques to perform linear stability analyses of coupled FSI problems.

In this paper, we propose a method that extends Chiba's approach (Chiba, 1998) to study the coupled dynamics of flow-structure systems. A time-stepping iterative procedure, based on the exponential transformation of the Jacobian matrix, was derived in a general setting. This was implemented within an existing immersed boundary solver and
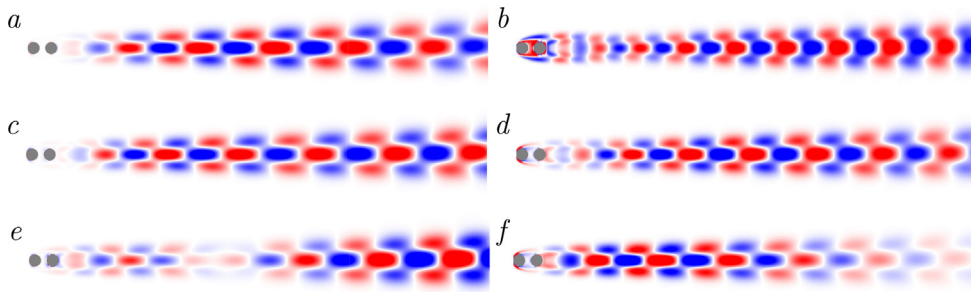
Fig. 14. Flow past two spring-mounted circular cylinders in tandem arrangement at $Re = 100$. Spatial distribution of the vorticity of the real part of mode 1 (a, c, e) and mode 2 (b, d, f) for $U^* = 4$ (a, b), $U^* = 5$ (c, d) and $U^* = 6$ (e, f).

validated against well-documented cases of flow-induced vibrations of rigid bodies. The outcomes of the linear stability analysis showed a good overall agreement with the results from the literature, obtained using mesh-conforming methods. Future developments of the method could include a local grid refinement to achieve a higher resolution near the immersed surface at a lower cost (Vanella et al., 2010). The validation tests were limited to the case of rigid-body motion, nevertheless, it is straightforward to extend the range of applicability of the method to deformable structures.

The matrix-free nature of the algorithm makes it particularly convenient for the analysis of three-dimensional flows around structures with complex geometries, where an analytical linearization of the coupled systems of equations would be impracticable. Moreover, the Cartesian grid employed within the IB framework facilitates the parallelization of the numerical scheme, which is an essential feature for solving three-dimensional problems within a reasonable time.

In Section 3.3, the method was tested on the case of two oscillating cylinders in tandem; the results of the stability analysis matched reasonably well with the nonlinear simulations, providing further confidence in the robustness of the method and opening the way to the instability analysis of multi-body configurations. Two dominant modes were identified across the range $3 \leq U^* \leq 14$. For values of the reduced velocity $U^* < 4$, only one mode is unstable and the cylinders oscillate out of lock-in. At $U^* = 4$ the second mode loses its stability and the cylinders enter the lock-in zone, then for $U^* = 5$ the modes cross and their interaction gives rise to the beating phenomenon observed in the nonlinear simulations. For $U^* > 5$ the growth rate of the dominant mode is significantly greater than that of the other one, justifying the higher amplitude of vibration observed in the calculations. The comparison with the linear stability of the fixed-free configuration shows that the mechanism giving rise to large amplitude oscillations is already present in the latter case, as the growth rate of the unstable mode grows in a similar fashion for $U^* > 5$, while its frequency is always close to that of the stationary wake mode. This observation implies that the vortex-shedding plays a major role in triggering the vibrations and that interference effects between the cylinders come into play only when the vertical separation between the two cylinders is large enough, as suggested by Borazjani and Sotiropoulos (2009).

One major advantage of the methodology consists of the generality of the formulation, which does not depend on the specific time-stepping scheme chosen for integrating the governing equations. Without the pretense of being exhaustive, in Section 2.3.2, some guidelines were provided for the selection of the linearization parameters, with the purpose to furnish the reader with the necessary tools to implement the strategy within existing CFD codes.

CRediT authorship contribution statement

Antonia Tirri: Conceptualization, Methodology, Software development, Computations, Validation, Writing – original draft, Reviewing and editing. **Alessandro Nitti:** Conceptualization, Software development, Writing – review & editing. **Javier Sierra-Ausin:** Conceptualization, Software development, Writing – review & editing. **Flavio Giannetti:** Conceptualization, Supervision, Writing – review & editing. **Marco D. de Tullio:** Conceptualization, Supervision, Software development, Writing – review & editing.

Declaration of competing interest

The authors declare that they have no known competing financial interests or personal relationships that could have appeared to influence the work reported in this paper.

Data availability

Data will be made available on request.

Appendix A. Derivation of the Gateaux derivative

In this section, we report further details of the derivation of Eq. (24) presented in Section 2.3.1.
Combining the definitions of $\boldsymbol{F}$ and $\boldsymbol{R}(\boldsymbol{q})$ given in Section 2, we get

$$\boldsymbol{F}(\boldsymbol{q}(t_0), T) = \int_{t_0}^{t_0+T} \boldsymbol{R}(\boldsymbol{q}(t))dt + \boldsymbol{q}(t_0). \tag{A.1}$$

We now consider the second term on the right-hand side of Eq. (23). Substituting the expression above, it reads

$$\left. \frac{\partial \boldsymbol{F}(\boldsymbol{q}, T)}{\partial \boldsymbol{q}} \right|_{\boldsymbol{q}_b} \boldsymbol{q}'(t_0) = \left. \frac{\partial}{\partial \boldsymbol{q}} \right|_{\boldsymbol{q}_b} \left[\int_{t_0}^{t_0+T} \boldsymbol{R}(\boldsymbol{q})dt \right] \boldsymbol{q}'(t_0) + \boldsymbol{q}'(t_0). \tag{A.2}$$

Recognizing that the extremes of integration do not depend on $\boldsymbol{q}$ and that $\boldsymbol{q}'(t_0)$ does not depend on time, we can interchange integration and differentiation and bring $\boldsymbol{q}'(t_0)$ inside the integral,

$$\left. \frac{\partial \boldsymbol{F}(\boldsymbol{q}, T)}{\partial \boldsymbol{q}} \right|_{\boldsymbol{q}_b} \boldsymbol{q}'(t_0) = \int_{t_0}^{t_0+T} \left. \frac{\partial \boldsymbol{R}(\boldsymbol{q})}{\partial \boldsymbol{q}} \right|_{\boldsymbol{q}_b} \boldsymbol{q}'(t_0)dt + \boldsymbol{q}'(t_0). \tag{A.3}$$

Supposing then a little variation of $\boldsymbol{q}'(t)$ in the interval $[t_0, t_0 + T]$, which is true for small values of T, we have replaced $\boldsymbol{q}'(t_0)$ into the integral with $\boldsymbol{q}'(t)$.

$$\int_{t_0}^{t_0+T} \left. \frac{\partial \boldsymbol{R}(\boldsymbol{q})}{\partial \boldsymbol{q}} \right|_{\boldsymbol{q}_b} \boldsymbol{q}'(t_0)dt \approx \int_{t_0}^{t_0+T} \boldsymbol{J}(\boldsymbol{q}_b)\boldsymbol{q}'(t)dt. \tag{A.4}$$

Finally, we recognize that (A.4) is simply the integration of the initial value problem given by Eq. (17), and therefore

$$\left. \frac{\partial \boldsymbol{F}(\boldsymbol{q}, T)}{\partial \boldsymbol{q}} \right|_{\boldsymbol{q}_b} \boldsymbol{q}'(t_0) \approx \boldsymbol{q}'(t_0 + T) - \boldsymbol{q}'(t_0). \tag{A.5}$$

Appendix B. Grid convergence tests

To assess the grid and domain convergence of the stability results, eigenvalue computations were performed on different grids for the VIV case presented in Section 3.2, with $(\rho^*, U^*) = (20, 7)$.

Table B.2 reports the growth rate λ and the Strouhal number St of the least stable eigenvalue for four different discretizations of the same domain of size $[-28D : 52D] \times [-28D : 28D]$, with the origin placed on the cylinder axis. On the rightmost column, it is reported the percentage error $e_{\%j}$ made in computing the eigenvalue ω_j, as the finest grid is taken as reference,

$$e_{\%j} = \frac{|\omega_j - \omega_{ref}|}{|\omega_{ref}|} \times 100. \tag{B.1}$$

Table B.3 reports the growth rate and the non-dimensional frequency of both the fluid and elastic modes for three distinct domains. The corresponding grids are coincident in the uniformly spaced rectangular zone around the cylinder, the minimum spacing being equal to $\Delta x_{min} = 0.022$. In particular, the grid used for the medium domain $D2$ corresponds to grid 2 in Table B.2. The analysis shows a minor difference between the medium and big domains, thus motivating the choice of $D2$ as the computational domain for the cases presented in Section 3.2. The blockage ratio reported in Table B.3 is defined as the ratio of the cylinder diameter to the cross-stream dimension of the computational domain.

Appendix C. Effect of the linearization parameter ϵ_0

To evaluate the influence of the user-defined linearization parameter ϵ_0 on the accuracy of the results, we report in Fig. C.1 the variation of the relative error e_r and the residual $\|\boldsymbol{r}\|$ of the least stable Ritz pair against ϵ_0. The former is given by

$$e_r = \frac{|\omega - \omega_{ref}|}{|\omega_{ref}|}, \tag{C.1}$$

where ω is the least stable eigenvalue computed for a given value of ϵ_0 on the chosen grid and ω_{ref} is a reference value. In the absence of an exact solution of the EVP, the selected ω_{ref} is the least stable eigenvalue computed on a reference grid with the parameter ϵ_0 chosen so as to minimize the residual $\|\boldsymbol{r}\|$. The results displayed in Fig. C.1 refer to the VIV case introduced in Section 3.2 with $(Re, \rho^*, U^*) = (60, 20, 7)$.

Table B.2

Convergence study with respect to grid resolution. For each of the four grids, the total number of cells N_c and the minimum cell dimension Δx_{min} are reported, together with the growth rate λ and the Strouhal number St of the least stable mode for $(Re, \rho^*, U^*) = (60, 20, 7)$. Grid 2 was used to obtain the results presented throughout the manuscript, while the relative error $e_\%$ is computed with respect to the values obtained with grid 4.

Grid	N_c	Δx_{min}	λ	St	$e_\%$
1	310 800	0.0286	0.0427	0.1205	0.662
2	513 000	0.0220	0.0447	0.1210	0.221
3	765 600	0.0182	0.0448	0.1211	0.106
4	1 068 600	0.0154	0.0447	0.1213	–

Table B.3

Sensitivity of the rightmost eigenvalues to the size of the computational domain for $(Re, \rho^*, U^*) = (60, 20, 7)$. D1: $[-35:65] \times [-35:35]$, D2: $[-28:52] \times [-28:28]$, D3: $[-21:39] \times [-21:21]$. All the grids used for the analysis have the same minimum cell dimension Δx_{min}. The percentage blockage ratio is reported for each domain size.

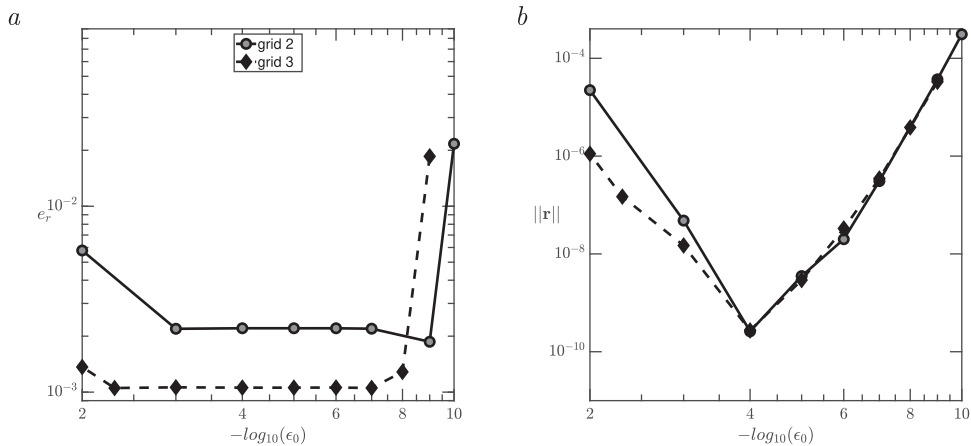|	D1 1.43%		D2 1.78%		D3 2.38%	
	λ_r	St	λ_r	St	λ_r	St
FM	0.0440	0.1206	0.0447	0.1210	0.0461	0.1219
EM	0.0086	0.1309	0.0085	0.1309	0.0080	0.1308

Fig. C.1. Effect of the input parameter ϵ_0 on the relative error (a) and direct residual (b) for the VIV case reported in Section 3.2 with the following set of parameters ($\rho^* = 20$, $Re = 60$, $U^* = 7$). Results are reported for two different grids (see Table B.2 for details), the relative error is computed with respect to the finest grid in Table B.2.

References

An, H.-B., Wen, J., Feng, T., 2011. On finite difference approximation of a matrix-vector product in the Jacobian-free Newton–Krylov method. J. Comput. Appl. Math. 236 (6), 1399–1409. http://dx.doi.org/10.1016/j.cam.2011.09.003.

Asgharzadeh, H., Borazjani, I., 2017. A Newton–Krylov method with an approximate analytical Jacobian for implicit solution of Navier–Stokes equations on staggered overset-curvilinear grids with immersed boundaries. J. Comput. Phys. 331, 227–256. http://dx.doi.org/10.1016/j.jcp.2016.11.033.

Borazjani, I., 2013. Fluid–structure interaction, immersed boundary-finite element method simulations of bio-prosthetic heart valves. Comput. Methods Appl. Mech. Engrg. 257, 103–116. http://dx.doi.org/10.1016/j.cma.2013.01.010.

Borazjani, I., Sotiropoulos, F., 2009. Vortex-induced vibrations of two cylinders in tandem arrangement in the proximity–wake interference region. J. Fluid Mech. 621, 321–364. http://dx.doi.org/10.1017/S0022112008004850.

Breugem, W.-P., 2012. A second-order accurate immersed boundary method for fully resolved simulations of particle-laden flows. J. Comput. Phys. 231, 4469–4498. http://dx.doi.org/10.1016/j.jcp.2012.02.026.

Chiba, S., 1998. Global stability analysis of incompressible viscous flow. J. Jpn. Soc. Comput. Fluid Dyn. 7, 20–48, (In Japanese).

Citro, V., Luchini, P., Giannetti, F., Auteri, F., 2017. Efficient stabilization and acceleration of numerical simulation of fluid flows by residual recombination. J. Comput. Phys. 344, 234–246. http://dx.doi.org/10.1016/j.jcp.2017.04.081.

Cossu, C., Morino, L., 2000. On the instability of a spring-mounted circular cylinder in a viscous flow at low Reynolds numbers. J. Fluids Struct. 14 (2), 183–196. http://dx.doi.org/10.1006/jfls.1999.0261.

de Tullio, M., De Palma, P., Iaccarino, G., Pascazio, G., Napolitano, M., 2007. An immersed boundary method for compressible flows using local grid refinement. J. Comput. Phys. 225 (2), 2098–2117. http://dx.doi.org/10.1016/j.jcp.2007.03.008, URL https://www.sciencedirect.com/science/article/pii/S0021999107001222.

Doaré, O., Michelin, S., 2011. Piezoelectric coupling in energy-harvesting fluttering flexible plates: linear stability analysis and conversion efficiency. J. Fluids Struct. 27 (8), 1357–1375. http://dx.doi.org/10.1016/j.jfluidstructs.2011.04.008.

Durbin, P., Iaccarino, G., 2002. An approach to local refinement of structured grids. J. Comput. Phys. 181 (2), 639–653. http://dx.doi.org/10.1006/jcph.2002.7147, URL https://www.sciencedirect.com/science/article/pii/S0021999102971470.

Eriksson, L.E., Rizzi, A., 1985. Computer-aided analysis of the convergence to steady state of discrete approximations to the euler equations. J. Comput. Phys. 57 (1), 90–128. http://dx.doi.org/10.1016/0021-9991(85)90054-3.

Fadlun, E., Orlandi, P., Mohd-Yusof, J., 2000. Combined immersed-boundary finite-difference methods for three-dimensional complex flow simulations. J. Comput. Phys. 161, 35–60. http://dx.doi.org/10.1006/jcph.2000.6484.

Fernández, M.A., Le Tallec, P., 2002. Linear stability analysis in fluid-structure interaction with transpiration. Part I: formulation and mathematical analysis. Research Report RR-4570, INRIA.

Förster, C., Wall, W., Ramm, E., 2007. Artificial added mass instabilities in sequential staggered coupling of nonlinear structures and incompressible viscous flows. Comput. Methods Appl. Mech. Engrg. 196, 1278–1293. http://dx.doi.org/10.1016/j.cma.2006.09.002.

Goldhirsch, L., Orszag, S., Maulik, B., 1987. An efficient method for computing leading eigenvalues and eigenvectors of large asymmetric matrices. J. Sci. Comput. 2 (1), 33–58. http://dx.doi.org/10.1007/BF01061511.

Gómez, F., Gomez, R., Theofilis, V., 2011. Coupling time-stepping numerical methods and standard aerodynamics codes for instability analysis of flows in complex geometries. In: 6th AIAA Theoretical Fluid Mechanics Conference. http://dx.doi.org/10.2514/6.2011-3753.

Gómez, F., Pérez, J.M., Blackburn, H.M., Theofilis, V., 2015. On the use of matrix-free shift-invert strategies for global flow instability analysis. Aerosp. Sci. Technol. 44, 69–76. http://dx.doi.org/10.1016/j.ast.2014.11.003, Instability and Control of Massively Separated Flows.

Goza, A., Colonius, T., Sader, J.E., 2018. Global modes and nonlinear analysis of inverted-flag flapping. J. Fluid Mech. 857, 312–344. http://dx.doi.org/10.1017/jfm.2018.728.

Griffith, M.D., Lo Jacono, D., Sheridan, J., Leontini, J.S., 2017. Flow-induced vibration of two cylinders in tandem and staggered arrangements. J. Fluid Mech. 833, 98–130. http://dx.doi.org/10.1017/jfm.2017.673.

Grouthier, C., Michelin, S., Bourguet, R., Modarres-Sadeghi, Y., de Langre, E., 2014. On the efficiency of energy harvesting using vortex-induced vibrations of cables. J. Fluids Struct. 49, http://dx.doi.org/10.1016/j.jfluidstructs.2014.05.004.

Knoll, D., Keyes, D., 2004. Jacobian-free Newton–Krylov methods: a survey of approaches and applications. J. Comput. Phys. 193 (2), 357–397. http://dx.doi.org/10.1016/j.jcp.2003.08.010.

Kornecki, A., Dowell, E., O'Brien, J., 1976. On the aeroelastic instability of two-dimensional panels in uniform incompressible flow. J. Sound Vib. 47 (2), 163–178. http://dx.doi.org/10.1016/0022-460X(76)90715-X.

Lãcis, U., Taira, K., Bagheri, S., 2016. A stable fluid–structure-interaction solver for low-density rigid bodies using the immersed boundary projection method. J. Comput. Phys. 305, 300–318. http://dx.doi.org/10.1016/j.jcp.2015.10.041.

chih Lai, M., Peskin, C.S., 2000. An immersed boundary method with formal second-order accuracy and reduced numerical viscosity. J. Comput. Phys. 705–719.

Lehoucq, R.B., Sorensen, D.C., Yang, C., 1998. ARPACK Users' Guide. Society for Industrial and Applied Mathematics, http://dx.doi.org/10.1137/1.9780898719628, arXiv:https://epubs.siam.org/doi/pdf/10.1137/1.9780898719628.

Mack, C.J., Schmid, P.J., 2010. A preconditioned krylov technique for global hydrodynamic stability analysis of large-scale compressible flows. J. Comput. Phys. 229 (3), 541–560. http://dx.doi.org/10.1016/j.jcp.2009.09.019.

Mansoorzadeh, S., Javanmard, E., 2014. An investigation of free surface effects on drag and lift coefficients of an autonomous underwater vehicle (AUV) using computational and experimental fluid dynamics methods. J. Fluids Struct. 51, http://dx.doi.org/10.1016/j.jfluidstructs.2014.09.001.

Meliga, P., Chomaz, J.-M., 2011. An asymptotic expansion for the vortex-induced vibrations of a circular cylinder. J. Fluid Mech. 671, 137–167. http://dx.doi.org/10.1017/S0022112010005550.

Mettot, C., Renac, F., Sipp, D., 2014. Computation of eigenvalue sensitivity to base flow modifications in a discrete framework: Application to open-loop control. J. Comput. Phys. 269, 234–258. http://dx.doi.org/10.1016/j.jcp.2014.03.022.

Moulin, J., Bonnet, P., Pfister, J.-L., Carini, M., Marquet, O., 2017. A distributed Lagrangian multiplier/fictitious domain approach for coupled fluid/structure stability analysis. In: 12th ERCOFTAC SIG 33 Workshop, Progress in Flow Instablity, Transition and Control (Certosa Di Pontignano, Italy).

Navrose, Mittal, S., 2016. Lock-in in vortex-induced vibration. J. Fluid Mech. 794, 565–594. http://dx.doi.org/10.1017/jfm.2016.157.

Negi, P.S., Hanifi, A., Henningson, D.S., 2020. On the linear global stability analysis of rigid-body motion fluid–structure-interaction problems. J. Fluid Mech. 903, A35. http://dx.doi.org/10.1017/jfm.2020.685.

Nitti, A., De Cillis, G., de Tullio, M., 2022. Cross-flow oscillations of a circular cylinder with mechanically coupled rotation. J. Fluid Mech. 943, A30. http://dx.doi.org/10.1017/jfm.2022.442.

Nitti, A., Kiendl, J., Reali, A., de Tullio, M., 2020. An immersed-boundary/isogeometric method for fluid–structure interaction involving thin shells. Comput. Methods Appl. Mech. Engrg. 364, 112977. http://dx.doi.org/10.1016/j.cma.2020.112977.

Papaioannou, G.V., Yue, D.K.P., Triantafyllou, M.S., Karniadakis, G.E., 2006. Three-dimensionality effects in flow around two tandem cylinders. J. Fluid Mech. 558, 387–413. http://dx.doi.org/10.1017/S0022112006000139.

Pfister, J.-L., Marquet, O., Carini, M., 2019. Linear stability analysis of strongly coupled fluid–structure problems with the arbitrary-Lagrangian–Eulerian method. Comput. Methods Appl. Mech. Engrg. 355, 663–689. http://dx.doi.org/10.1016/j.cma.2019.06.024.

Prasanth, T., Mittal, S., 2009. Vortex-induced vibration of two circular cylinders at low Reynolds number. J. Fluids Struct. 25, 731–741. http://dx.doi.org/10.1016/j.jfluidstructs.2008.12.002.

Sabino, D., Fabre, D., Leontini, J.S., Jacono, D.L., 2020. Vortex-induced vibration prediction via an impedance criterion. J. Fluid Mech. 890, http://dx.doi.org/10.1017/jfm.2020.104.

Schulze, J.C., Schmid, P.J., Sesterhenn, J.L., 2009. Exponential time integration using Krylov subspaces. Internat. J. Numer. Methods Fluids 60 (6), 591–609. http://dx.doi.org/10.1002/fld.1902, arXiv:https://onlinelibrary.wiley.com/doi/pdf/10.1002/fld.1902.

Seo, J.H., Mittal, R., 2011. A sharp-interface immersed boundary method with improved mass conservation and reduced spurious pressure oscillations. J. Comput. Phys. 230, 7347–7363. http://dx.doi.org/10.1016/j.jcp.2011.06.003.

Siconolfi, L., Citro, V., Giannetti, F., Camarri, S., Luchini, P., 2017. Towards a quantitative comparison between global and local stability analysis. J. Fluid Mech. 819, 147–164. http://dx.doi.org/10.1017/jfm.2017.167.

Singh, S., Mittal, S., 2005. Vortex-induced oscillations at low Reynolds numbers: Hysteresis and vortex-shedding modes. J. Fluids Struct. 20, 1085–1104. http://dx.doi.org/10.1016/j.jfluidstructs.2005.05.011.

Sorensen, D.C., 1992. Implicit application of polynomial filters in a k-step Arnoldi method. SIAM J. Matrix Anal. Appl. 13, 357–385.

Tangorra, J.L., Davidson, S.N., Hunter, I.W., Madden, P.G.A., Lauder, G.V., Dong, H., Bozkurttas, M., Mittal, R., 2007. The development of a biologically inspired propulsor for unmanned underwater vehicles. IEEE J. Ocean. Eng. 32 (3), 533–550. http://dx.doi.org/10.1109/JOE.2007.903362.

Tezuka, A., Suzuki, K., 2006. Three-dimensional global linear stability analysis of flow around a spheroid. AIAA J. 44 (8), 1697–1708. http://dx.doi.org/10.2514/1.16632, arXiv:https://doi.org/10.2514/1.16632.

Theodorsen, T., 1934. General theory of aerodynamic instability and the mechanism of flutter.

Theofilis, V., 2011. Global linear instability. Annu. Rev. Fluid Mech. 43 (1), 319–352. http://dx.doi.org/10.1146/annurev-fluid-122-160705, arXiv:https://doi.org/10.1146/annurev-fluid-122109-16070.

Theofilis, V., Colonius, T., 2011. Special issue on global flow instability and control. Theor. Comput. Fluid Dyn. 25, 1–6. http://dx.doi.org/10.1007/s00162-010-0217-3.

de Tullio, M.D., Cristallo, A., Balaras, E., Verzicco, R., 2009. Direct numerical simulation of the pulsatile flow through an aortic bileaflet mechanical heart valve. J. Fluid Mech. 622, 259–290. http://dx.doi.org/10.1017/S0022112008005156.

Uhlmann, M., 2003. First experiments with the simulation of particulate flows.

Uhlmann, M., 2005. An immersed boundary method with direct forcing for the simulation of particulate flows. J. Comput. Phys. 209 (2), 448–476. http://dx.doi.org/10.1016/j.jcp.2005.03.017.

Vanella, M., Balaras, E., 2009. A moving-least-squares reconstruction for embedded-boundary formulations. J. Comput. Phys. (Print) 228 (18), 6617–6628.

Vanella, M., Rabenold, P., Balaras, E., 2010. An embedded-boundary method with adaptive mesh refinement for fluid-structure interactions problems. J. Comput. Phys. 229, 6427–6449. http://dx.doi.org/10.1016/j.jcp.2010.05.003.

Yang, J., Balaras, E., 2006. An embedded-boundary formulation for large-eddy simulation of turbulent flows interacting with moving boundaries. J. Comput. Phys. 215, 12–40. http://dx.doi.org/10.1016/j.jcp.2005.10.035.

Yang, X., Zhang, X., Li, Z., He, G.-W., 2009. A smoothing technique for discrete delta functions with application to immersed boundary method in moving boundary simulations. J. Comput. Phys. 228, 7821–7836. http://dx.doi.org/10.1016/j.jcp.2009.07.023.